1 **An alveolus lung-on-a-chip model of *Mycobacterium fortuitum* lung infection**

2 Victoria Ektnitphong[1], Beatriz R.S. Dias[1], Priscila C. Campos[1] and Michael U. Shiloh[1,2]

3 [1]Department of Internal Medicine and [2]Department of Microbiology

4 University of Texas Southwestern Medical Center

5 5323 Harry Hines Blvd., Y9.308

6 Dallas, TX 75390-9113

7 Corresponding author: Michael.shiloh@utsouthwestern.edu

ABSTRACT

Lung disease due to non-tuberculous mycobacteria (NTM) is rising in incidence. While both two dimensional cell culture and animal models exist for NTM infections, a major knowledge gap is the early responses of human alveolar and innate immune cells to NTM within the human alveolar microenvironment. Here we describe development of a humanized, three-dimensional, alveolus lung-on-a-chip (ALoC) model of *Mycobacterium fortuitum* lung infection that incorporates only primary human cells such as pulmonary vascular endothelial cells in a vascular channel, and type I and II alveolar cells and monocyte-derived macrophages in an alveolar channel along an air-liquid interface. *M. fortuitum* introduced into the alveolar channel primarily infected macrophages, with rare bacteria inside alveolar cells. Bulk-RNA sequencing of infected chips revealed marked upregulation of transcripts for cytokines, chemokines and secreted protease inhibitors (SERPINs). Our results demonstrate how a humanized ALoC system can identify critical early immune and epithelial responses to *M. fortuitum* infection. We envision potential application of the ALoC to other NTM and for studies of new antibiotics.

22 **INTRODUCTION**

23 Nontuberculous mycobacteria (NTM) represent a diverse group of environmental organisms
24 found in varied natural habitats such as soil, water, and vegetation (Mercaldo et al., 2023).
25 Traditionally considered opportunistic pathogens of people with structural or immune deficits, lung
26 disease secondary to NTM is increasing in incidence in women and people over 65 years of age
27 (Winthrop et al., 2020). Among the NTM, *M. fortuitum* is the second most frequently encountered
28 rapidly-growing NTM after *Mycobacterium abscessus*, and can cause a spectrum of infections
29 including pulmonary, skin and soft tissue, and disseminated infections (Roquet-Baneres et al.,
30 2023, Kim et al., 2023). NTM lung infections are more frequent and more severe in
31 immunocompromised individuals and individuals with pre-existing conditions such as
32 bronchiectasis, severe chronic obstructive pulmonary disease (COPD), cystic fibrosis, organ
33 transplant and cancer (Roquet-Baneres et al., 2023, Kim et al., 2023). Treatment of NTM lung
34 disease can be complex due to the presence of antibiotic resistance, medication side effects and
35 extended duration of drug treatment. More efforts are needed to develop new, safe and efficacious
36 therapeutics and to shorten treatment duration (Johansen and Kremer, 2020, Orme and Ordway,
37 2014, Kremer, 2020). In addition, the rising incidence of NTM lung infections among individuals
38 without defined predisposing conditions indicates that a greater understanding of the immune
39 response to NTM lung infection is needed.

40 Expanding the scope of knowledge of the dynamic interactions between humans and NTM is
41 essential for developing effective prevention and treatment strategies for NTM lung disease, but
42 gaining such knowledge has been hindered by the lack of suitable *in vitro* and *in vivo* models of
43 NTM lung infection (Baldwin et al., 2019). Current *in vitro* models typically use traditional two-
44 dimensional cell culture methods with primary human $CD14^+$ peripheral blood-derived
45 macrophages or immortalized monocytic cell lines THP-1 and U937 (Kilinc et al., 2022), and
46 alveolar epithelial cell lines such as A549 (Rampacci et al., 2020). Although immortalized cell lines

allow for large-scale screening and assay reproducibility, a major disadvantage is that they may not completely replicate myeloid cell responses in humans, especially in the unique alveolar microenvironment. For example, the use of PMA to differentiate THP-1 and U937 cells into adherent macrophage-like cells alters monocytic surface markers, transcriptional activities, and cytokine production (Rampacci et al., 2020). Animal models have also been established to study host immune responses to NTM and for testing potential antimicrobial compounds and vaccines. Most animal models of NTM lung infection use mice as the host species including for *M. abscessus* (Caverly et al., 2015, De Groote et al., 2014) and *Mycobacterium avium* (Gonzalez-Perez et al., 2013, Gangadharam, 1995). However, the variable virulence of NTM in model organisms makes establishing consistent animal models challenging. For example, *M. avium* can establish a productive lung infection in immunocompetent mice, whereas *M. abscessus* is typically rapidly cleared and requires immunocompromised mice to achieve a similar outcome (Chan et al., 2016). Animal models for other NTM species such as *M. fortuitum* are lacking, delaying progress towards understanding shared and unique molecular mechanisms of pathogenicity for various NTM. Thus, developing *in vitro* models that can recapitulate the human lung microenvironment using primary human cells has the potential to advance the study of pulmonary NTM infections, and is a critical step towards developing improved prevention, vaccine and treatment strategies.

The alveolus lung-on-a-chip (ALoC) is an innovative microfluid device composed of microfabricated channels and chambers that mimic the architecture and cellular composition of the lung alveolus, the initial site of interaction for pulmonary NTM infection (Bethencourt et al., 2024) . The “chip” contains two overlapping channels, parallel to each other, that are separated by a porous membrane. It features alveolar epithelial cells lining one channel and pulmonary microvascular endothelial cells (HMVECs) lining the other to closely replicate the alveolar-capillary interface of the human lung (Dasgupta et al., 2023). Because the cell types grow in

distinct channels, media or air flow through the channels can be independently controlled to create distinct environments for the cells. Additional advantages of the ALoC include the ability to generate an air-liquid interphase (ALI) that is hallmark of the alveolus and application of mechanical stretch that is essential for the proper differentiation of alveolar epithelial cells into type I (AT1) and type II (AT2) pneumocytes. In that respect, the ALoC helps overcome one of the major obstacles of *in vitro* studies of alveolar epithelial cells, namely, simultaneously differentiating both AT1 and AT2 cells in culture by leveraging stretch and growth factor addition (Li et al., 2018). Thus, compared to traditional tissue culture methods, the ALoC system provides a more physiologically relevant environment to study cells and pathogens of the human lung and has been applied to several airway diseases and pathogens including influenza A virus (Bai et al., 2022, Haiqing Bai et al., 2022), *Mycobacterium tuberculosis* (Thacker et al., 2020), and acute radiation induced lung injury (RILI) (Dasgupta et al., 2023).

The complex interaction between *M. fortuitum* and the human alveolar epithelial and immune cells remains poorly understood. Here, we develop and use a fully humanized ALoC model as a platform to study the host-pathogen interactions of *M. fortuitum* within the alveolar microenvironment. By recapitulating key features of the alveolar interface, including cellular composition, mechanical forces, and biochemical gradients, this model offers a unique opportunity to investigate the dynamics of *M. fortuitum* infection in a controlled and reproducible manner. Through integration of advanced imaging techniques and transcriptomic analyses, we identify macrophages as the primary cell type infected in the alveolus and upregulation of several inflammatory pathways after *M. fortuitum* infection of the humanized ALoC. We propose application of the humanized alveolus lung-on-a-chip as a new model to study NTM infections.

RESULTS

Two types of lung chips have been developed to date, one that approximates a bronchial airway (Benam et al., 2015, Benam et al., 2016) and another more like an alveolus (**Figure 1A**) (Huh et

97 al., 2012a, Huh et al., 2010, Huh et al., 2012b). Since early NTM infection occurs in the alveolus,
98 we chose the alveolus lung-on-a-chip (ALoC) as our working model for NTM infection (**Figure**
99 **1B**), as previously demonstrated with *E. coli* (Huh et al., 2010). We initially decided to use *M.*
100 *fortuitum* to model airway NTM infection using the ALoC model both because it is rapidly-growing,
101 with a doubling time of 2-3 hours (Qin et al., 1999), and because amongst the rapid growers it
102 has one of the highest age-adjusted incidence of disease (Donohue, 2021).

103 Constructing a functional ALoC requires meticulously following a stepwise protocol
104 (**Supplemental Figure 1A**). Briefly, the membranes of individual chips are chemically activated,
105 coated with extracellular matrix and then human alveolar epithelial cells are added to the air (or
106 apical) channel. After three days, human primary lung microvascular endothelial cells are
107 introduced to the vascular (or basal) channel. Once cells are confluent (~1 day), the alveolus-on-
108 a-chip is connected to regulated media flow (30 uL/hr) in both channels. The next day, the apical
109 channel media is removed, generating an air-liquid interface (ALI), and after 2 days of ALI, stretch
110 is introduced to mimic breathing (5% stretch intensity, 0.2 Hz) and induce surfactant production
111 (Thacker et al., 2020). After two days of stretch we add differentiated human $CD14^+$ peripheral
112 blood-derived macrophages (hereafter called 'macrophages') from anonymous donors to the top
113 channel (**Figure 1C**). To assess the donor compatibility of the alveolar epithelial cells and
114 macrophages in the apical channel, we used immunofluorescence to compare AT1 and AT2 cell
115 differentiation, cell morphology and distribution of cells along the apical channel of ALoCs with
116 and without macrophages. In ALoCs without macrophages, a monolayer of both AT1 and AT2 cell
117 types was distributed equally across the apical channel (**Figure 1D, Supplemental Figure 1B**).
118 High resolution images of ALoCs without macrophages highlighted distinct AT1 and AT2 cell types
119 after 15 days in culture on the ALoC (**Figure 1E**). Three-dimensional reconstruction of the ALoC
120 contrasted the cuboidal, cobblestone morphology of AT2 cells to the flat, squamous morphology
121 of AT1 cells (**Figure 1F**). Cross sectional imaging of the airway channel further highlighted the

122 nuclei in the basal region of the apical channel with interspersed AT1 and AT2 cells (**Figure 1G**).
123 In ALoCs with macrophages, we also observed a monolayer of differentiated AT1 and AT2 cells
124 with seeded macrophages residing on top of the alveolar epithelial monolayer (**Figure 1H-J**).
125 Since macrophages were added 2 days after 100% confluency of the apical channel, it is expected
126 that they would be found loosely attached to the alveolar epithelial layer rather than within the
127 alveolar epithelial layer. Although we introduced the same number of macrophages as alveolar
128 epithelial cells, we observed many fewer macrophages overall, suggesting that the majority failed
129 to adhere to the epithelial layer and were washed away or clumped together (**Supplemental**
130 **Figure 1C**). Stitched images of ALoCs containing macrophages showed that, despite losing many
131 macrophages, the remaining macrophages were sufficient to evenly distribute across the entire
132 apical channel (**Supplemental Figure 1D**). We also observed that despite the addition of
133 macrophages, AT cell distribution was comparable to uninfected ALoCs without macrophages. At
134 higher magnification, we observed rounded macrophages dispersed on top of the cuboidal
135 shaped AT2 cells (**Figure 1I**). Three-dimensional reconstruction of the apical channel also
136 demonstrated the same cuboidal morphology of AT2 cells and flat, squamous AT1 cells that we
137 observed in ALoCs without macrophages (**Figure 1J**). Cross-sectional imaging showed
138 macrophages residing predominantly on top of the alveolar epithelial monolayer (**Figure 1K**).
139 From these experimental observations, namely that AT1 and AT2 cell differentiation was
140 maintained after the addition of primary human $CD14^+$ peripheral blood macrophages, we
141 concluded that macrophages could safely be added to the human ALoC model without
142 dramatically altering epithelial biology.

143 After establishing the ALoC model with human macrophages, we next incorporated mCherry-
144 expressing *M. fortuitum* to the system. We introduced mCherry-expressing *M. fortuitum* at an
145 estimated multiplicity of infection (MOI) of ~1 for the approximate number of AT1 and AT2 cells on
146 the chip (~3.0×10^4) (**Figure 2A**). Because we used immunofluorescence to monitor different cell

147 types on the ALoC, uninfected ALoCs from the same experiment were used to confirm AT1 and
148 AT2 differentiation (**Supplemental Figure 2A**) and we observed similar trends of AT1 and AT2
149 differentiation. When ALoCs without macrophages were infected with *M. fortuitum*, we observed
150 appropriate AT2 cell distribution across the chip in addition to large clumps of bacteria scattered
151 across the ALoC (**Figure 2B**). Along the apical channel in *M. fortuitum*-infected ALoC, we
152 observed areas that had little to no immunofluorescence signal throughout the z-stack that we did
153 not observe in uninfected ALoCs with or without macrophages. In the areas on the ALoCs
154 containing "dark patches" lacking AT1 or AT2 immunofluorescence, we could not determine at
155 lower resolution if those areas were due to cell death, but higher resolution images of ALoCs
156 without macrophages after 24 hours of mCherry *M. fortuitum* infection suggested loss of viability
157 of AT1 and AT2 cells in areas adjacent to bacteria (**Figure 2C**). Three-dimensional reconstruction
158 of *M. fortuitum*-infected ALoCs without macrophages demonstrated many AT2 cells with a
159 cuboidal morphology but interestingly we also observed a more "flattened" AT2 morphology
160 (**Figure 2D**). Whether these are AT1 cells with HT2 signal or AT2 cells with flattened morphology
161 could not be determined. HT1 labeling was very diffuse in *M. fortuitum*-infected ALoCs and we
162 also observed co-staining of HT1 and HT2 in both alveolar epithelial cell types in *M. fortuitum*-
163 infected ALoCs without macrophages compared to uninfected ALoCs without macrophages
164 (**Supplemental Figure 2B-D**). High-resolution cross-sectional analysis bacterial clumps on the
165 *M. fortuitum*-infected ALoC without macrophages demonstrated bacteria interspersed amongst
166 AT1 and AT2 cells (**Figure 2E**). No *M. fortuitum* cord-like structures were observed within the
167 initial 24 hours of infection. Taken together, introducing *M. fortuitum* to the ALoC model at an
168 approximate MOI of 1 generated a productive infection without overwhelming the alveolar
169 channel.

170 We next wanted to determine how *M. fortuitum* grows on ALoC in the presence of human
171 macrophages. Twenty-four hours after seeding human macrophages onto the ALoC, we infected

172 ALoCs with macrophages with *M. fortuitum* as described above, using the same donors for
173 alveolar epithelial and pulmonary microvascular endothelial cell as for ALoCs without
174 macrophages (**Figure 3A**). On ALoCs infected with *M. fortuitum* 24 hours after macrophage
175 seeding, there was suitable distribution of AT2 cells across the chips (comparable to infected
176 ALoCs without macrophages). In contrast to ALoC lacking macrophages infected with *M.*
177 *fortuitum*, inclusion of macrophages resulted in most bacteria identified intracellularly within
178 macrophages with no apparent bacterial clumps (**Figure 3B**). The AT2 cell morphology appeared
179 more rounded in shape in areas adjacent to infected macrophages and AT2 cells remained intact
180 with no areas of apparent cell death as we observed in *M. fortuitum*-infected ALoCs without
181 macrophages (**Figure 3C**). Similarly to *M. fortuitum*-infected ALoCs without macrophages, we
182 again did not observe *M. fortuitum* cord-like structures. Of note, we were unable to image AT1
183 cells directly in infected ALoCs with macrophages due to limitations in the number of fluorophores
184 available in one experiment. Three-dimensional reconstruction highlighted the expected cuboidal
185 morphology of AT2 cells and demonstrated macrophage clusters near the chip edges (**Figure**
186 **3D**). We observed less "flattening" of the AT2 cells in ALoCs with macrophages but were not able
187 to directly assess AT1 cells in the infected ALoCs with macrophages to determine if they
188 demonstrated the same trends of AT1 and AT2 co-staining and AT1 signal diffusion. Cross-
189 sectional analysis of the ALoC with macrophages also highlighted that bacteria were intracellular
190 in macrophages and not residing on top of the macrophages (**Figure 3E**). In addition, by removing
191 the AT2 signal, we observed *M. fortuitum* within macrophages in a three-dimensional
192 reconstruction of the ALoC (**Figure 3F**). To quantify bacteria within either AT2 or $CD14^+$ cells, we
193 analyzed 10 z-stacks from 3 independent ALoCs containing macrophages. We used three-
194 dimensional reconstruction and ortho-projections to assign bacteria within AT2 cells ($HT2^+$) or
195 macrophages ($CD14^+$) and determined that bacteria were found more often in macrophages than
196 AT2 cells (**Figure 3G**). Taken together, we conclude that *M. fortuitum* infection of ALoC containing

197 macrophages results in a productive infection, and that ingestion of bacteria by macrophages may
198 protect adjacent epithelia from infection-induced cell death.

199 To determine the alveolar response to *M. fortuitum* infection using the human ALoC, we
200 determined the impact of *M. fortuitum* infection on ALoC with macrophages compared to
201 uninfected ALoC with macrophages using bulk RNA sequencing. After infection at an MOI of 1 for
202 24 hours, we collected total RNA from the apical channel containing AT1 cells, AT2 cells and
203 macrophages for sequencing. While there was some heterogeneity in the response, as would be
204 expected in a primary infection, we observed 1454 genes were more than 2-fold upregulated,
205 while 588 were downregulated more than 2-fold (**Figure 4A, B**). Amongst the upregulated genes,
206 we observed significant upregulation of key cytokines such as tumor necrosis factor (*TNF*),
207 granulocyte-macrophage colony-stimulating factor (*GM-CSF* or *CSF2*), macrophage colony-
208 stimulating factor (*M-CSF* or *CSF3*), interleukin 1A (*IL1A*), interleukin 1B (*IL1B*), interleukin 6 (*IL6*),
209 and interleukin 8 (*IL8*), along with the alarmin, calprotectin (*S100A8* and *S100A9*) (**Figure 4C**).
210 We also observed several chemokines upregulated including the chemokine (C-X-C motif) ligand
211 family members *CXCL1, CXCL2, CXCL3, CXCL5, CXCL6, CXCL10* and *CXCL11* and the C-C
212 motif chemokine ligand family members *CCL2, CCL5, CCL20* and *CCL28* (**Figure 4C**). Finally,
213 we also noted that many secreted serine protease inhibitor (SERPIN) genes were also
214 upregulated by *M. fortuitum* infection (**Figure 4D**). Using pathway analysis (Ge et al., 2018), we
215 found that the most significantly upregulated processes were involved in host defense including
216 “response to bacterium”, “defense response to bacterium”, “antimicrobial humoral response”,
217 “response to molecule of bacterial origin” and “response to lipopolysaccharide” (**Table 1**).
218 Likewise, upregulated molecular functions included several annotated as involved in “signaling”
219 in addition to “cytokine” and various channel functions (**Table 2**). Taken together, our data highlight
220 the acute inflammatory response of humanized ALoC containing human macrophages to *M.*
221 *fortuitum* infection.

Discussion

We report the development of a fully humanized ALoC model for alveolar NTM infection. This model develops features consistent with initial primary alveolar infection, including infection of both airway macrophages and occasional alveolar cells. Moreover, bulk RNA sequencing reveals activation of an acute inflammatory signaling cascade, including induction of cytokines, chemokines and alarmins like serpins and calprotectin, with potential roles in recruitment of myeloid and lymphoid cells from the vasculature and in triggering a robust immune response to restrict bacterial growth. These findings highlight the value of using the humanized lung on a chip to model a primarily human infectious disease.

Prior studies using the alveolus-on-a-chip have included infection models, such as infection with *E. coli* (Huh et al., 2010), *M. tuberculosis* (Thacker et al., 2020), *Aspergillus fumigatus* (Hoang et al., 2022), *Staphylococcus aureus* (Bai et al., 2022, Deinhardt-Emmer et al., 2020), and influenza virus (Bai et al., 2022, Deinhardt-Emmer et al., 2020). The alveolus-on-a-chip has also been used to determine the effect of mechanical strain on inflammation and particle uptake (Huh et al., 2010), pulmonary thrombosis (Jain et al., 2018), and mechanotransduction and pulmonary edema (Li et al., 2019). In the context of *M. tuberculosis* and *A. fumigatus* infection models, addition of human monocytes/macrophages impacts pathogenesis (Thacker et al., 2020, Hoang et al., 2022). With *M. tuberculosis*, cord-like structures are observed compressing macrophage nuclei (Mishra et al., 2023). We did not observe a similar phenomenon with *M. fortuitum* infection of human macrophages, which might be due to differences in the cell walls of the organisms or other factors that impact the growth characteristics of *M. tuberculosis* (slow) as compared to *M. fortuitum* (rapid). Alternatively, differences in the time after infection used for analysis (24 hours in this study versus 72 hours (Mishra et al., 2023)) or imaging techniques may also account for these differences.

246 We identified a transcriptional signature of early human alveolar infection with *M. fortuitum*. Some
247 notable findings include marked upregulation of important cytokines and chemokines that may be
248 involved in stimulating an early innate immune response to airway infection. For example, both
249 IL6 and IL8 are key cytokines involved in neutrophil recruitment to the airway (Fu and Harrison,
250 2021), and such recruited cells could have both beneficial (contributing to NTM killing) and
251 detrimental (involvement in tissue damage and bronchiectasis) effects (Alkarni et al., 2023).

252 While there have been previous studies of human peripheral blood transcriptional responses in
253 the context of pulmonary NTM infection (Wang et al., 2024, Cowman et al., 2018, Lindestam
254 Arlehamn et al., 2022) or tuberculosis (Tabone et al., 2021, Berry et al., 2010), as well as efforts
255 to determine transcriptional responses in human lung tissue from tuberculosis patients (Wang et
256 al., 2023a), to our knowledge this is the first analysis of the early interaction of an NTM with a
257 humanized ALoC. Interestingly, in the RNA sequencing analysis of PBMCs from individuals
258 infected with *M. avium*, TNF signaling was enriched, and individual genes such as those for
259 *SERPINA1* and calprotectin were modestly upregulated (Lindestam Arlehamn et al., 2022).
260 Likewise, in a proteomics analysis of serum exosomes in humans with NTM infection, a variety of
261 serpins including SERPINA1 and SERPINA5 were enriched in patients with *M. abscessus* or *M.*
262 *avium* infection (Wang et al., 2023b). Recent work has found the induction of cytosolic SERPINs
263 may protect *M. marinum* infected macrophages from cathepsin B mediated lysosomal rupture and
264 cell death (Nobs et al., 2024), a process called lysoptosis that is evolutionary conserved from *C.*
265 *elegans* to mammals (Luke et al., 2022). Thus, SERPIN induction by *M. fortuitum* infection,
266 potentially within infected macrophages, may act to protect infected cells from lysoptosis. Of note,
267 because we used bulk RNA sequencing, we were unable to identify the precise cellular source of
268 transcriptional changes identified in our analysis. Future single cell sequencing studies will be
269 necessary to determine the responses of individual cell types within the model system, and how

270 such responses impact intercellular communication. Taken together, our bulk RNAseq analysis
271 has identified unique features of early alveolar NTM infection.

272 There are several limitations to our model. First, because our model uses all primary human cells,
273 genetic manipulation of the various cellular constituents is impractical, though primary human
274 monocytes can be transduced with lentivirus to abrogate gene expression (Campbell and Spector,
275 2012, Franco et al., 2017). Alternatively, use of genetically modified human or mouse cell lines
276 can overcome this limitation, though immortalized cell lines have their own inherent drawbacks.
277 Second, because primary cells, whether pulmonary epithelial cells, pulmonary vascular cells or
278 PBMCs, are obtained from unique individuals, genetic variation generates greater complexity.
279 Finally, though our model does allow multiple cell types (epithelia, endothelia and myeloid cells)
280 to interact with each other and the NTM in the alveolar microenvironment, the interactions are
281 limited to the cells added to the chamber, and thus do not include all the possible myeloid and
282 lymphoid cells that could be recruited to the airway in the setting of pulmonary mycobacterial
283 disease, such as neutrophils (Kimmey et al., 2015), eosinophils (Bohrer et al., 2021) or innate
284 lymphoid cells (Ardain et al., 2019).

285 In conclusion, we have developed a fully humanized alveolus on a chip model of pulmonary NTM
286 infection. By capturing the complexity of NTM in three dimensions and with multiple cell types, as
287 would be found in a human lung, this model creates an opportunity to better characterize the
288 cellular and molecular mechanisms that mediate the outcome of human airway NTM infections.
289 Because NTM infections are on the rise, particularly in individuals with cystic fibrosis,
290 bronchiectasis and people with HIV, it may be useful to apply this technology to determine the
291 relative impact of genetic risk alleles (i.e. for those with cystic fibrosis) or coinfection with HIV on
292 the alveolar transcriptional responses or bacterial survival in the alveolus over time. Furthermore,
293 by leveraging this system to directly compare responses to other common human pulmonary NTM
294 infections, such as *M. avium* (Cristancho-Rojas et al., 2023, Varley and Winthrop, 2022, Donohue,

295 2021), *M. kansasii* and *M. abscessus* (Toure et al., 2023, Lagune et al., 2023, Cristancho-Rojas
296 et al., 2023, Ordway et al., 2008, Klever et al., 2023) future studies could identify shared and
297 unique survival strategies used by each organism, and establish distinct immune pathways
298 responsive to each pathogen which could function to limit or exacerbate infection, or be used
299 clinically as biomarkers of disease. Finally, as new drugs are developed to treat pulmonary NTM
300 infection, we envision applying this model for the simultaneous assessment of efficacy (i.e.
301 reduction in bacterial load) and cellular toxicity via infusion of test compounds into the vascular
302 channel.

303 **Materials and Methods**

304 **Bacteria**

305 *Mycobacterium fortuitum* subsp. *fortuitum* strain was obtained from ATCC (strain TMC 1529). We
306 transformed *M. fortuitum* with a vector containing *mCherry* driven by the GroEL constitutive
307 promoter.

308 **Primary Cell Culture**

309 Primary human alveolar epithelial cells (ATs) were obtained from Cell Biologics (H-6053). Prior to
310 seeding on Alveolus Lung-on-Chips (ALoCs), ATs were expanded *in vitro* in a T25 flask coated
311 with a 1% gelatin-based coating solution (Cell Biologics, catalog #6950) and complete medium
312 comprising of base media and supplements (Lonza, CC-3118). Medium was prepared according
313 to manufacturer's instructions using all supplements except GA-1000 where 1% Pen-Strep
314 solution (Gibco 15140-122) was added instead along with 5% FBS and hereby called Small
315 Airway Growth Medium (SAGM). Primary human microvascular endothelial cells were purchased
316 from Lonza (CC-2527). Human Lung Microvascular Endothelial cells (HMVECs) were expanded
317 in a T75 in complete medium comprising of base media and supplements (Lonza, CC-3202).
318 Medium was prepared according to manufacturer's instructions using all supplements except GA-

319 1000 where 1% Pen-Strep solution was used instead along with 5% FBS and hereby called EGM-
320 2MV. Both primary cell lines were cultured at 37°C in 5% CO_2 until ~80% confluency before
321 detachment with TrypLE Express (Gibco 12604013) and use on the ALoC.

322 One week prior to seeding the macrophages on the ALoC, peripheral blood mononuclear cells
323 (PBMCs) were obtained from buffy coat purchased from anonymous donors (Carter BloodCare).
324 PBMCs were isolated using Ficoll (Cytivia, 17144003) and SepMate50 tubes from StemCell
325 Technologies (85450). $CD14^+$ monocytes were positively selected from the PBMCs using CD14
326 Microbeads (Miltenyi, 130-050-201), and seeded onto uncoated petri dishes. The monocytes
327 were cultured overnight in RPMI medium (Gibco 11875-093) supplemented with 10% heat-
328 inactivated human serum obtained from the buffy coat of the donor, 1% HEPES buffered solution
329 (Lonza CC-5022), 1% sodium pyruvate (Gibco 11360-070), and 50 ng/mL human granulocyte-
330 macrophage colony-stimulating factor (GM-CSF) (Peprotech 300-03-100UG) and is hereby called
331 macrophage medium. The next day, the serum in the medium was changed to 10% FBS for the
332 remainder of the culturing. $CD14^+$ monocytes were differentiated to human monocyte-derived
333 macrophages (HMDMs) for 7 days at 37°C in 5% CO_2 until use on the ALoCs. GM-CSF was
334 added to medium for the first 4 days to differentiate the $CD14^+$ monocytes.

335 **Human Alveolus LoC Model**

336 ALoCs fabricated with polydimethylsiloxane (PDMS) were purchased from Emulate. The chips
337 were activated using a 0.5 mg/mL solution comprised of ER-1 and ER-2 (Emulate) that was
338 protected from light during the activation process. Working in a dark biosafety cabinet (BSC), both
339 the top and bottom channel were filled completely with ER-1/ER-2 and placed under a UV light
340 for 10 min, inspected for bubbles with a brightfield microscope and placed under the UV light for
341 an additional 10 min. After activation of all chips, the top and bottom channels were coated with
342 an extracellular matrix (ECM) solution specific to the cell type. The top channel (ATs) was coated
343 with an ECM solution containing Collagen IV at 200 µg/mL (Sigma C5533), Fibronectin at 30

344 μg/mL (Millipore Sigma F2006) and Laminin at 5μg/mL (Sigma L6274). The bottom channel
345 (endothelial cells) was coated with an ECM solution containing Collagen IV at 200 μg/mL and
346 Fibronectin at 30 μg/mL. All ECM components and solutions were kept on ice and prepared by
347 manufacturer's recommendations. With an empty 200 μL pipette tip plugged into each outlet port,
348 100 uL of ECM solution were added to the respective channels by expelling ECM solution from
349 pipette tip and plugging the inlet ports with the tip. The ECM-coated ALoCs were incubated at 4°C
350 overnight and the next day each channel was washed twice with 200 μL of respective medium.
351 Respective mediums were left in each channel prior to cell seeding and ALoCs were stored at
352 4°C until cell seeding.

353 ATs were seeded first in the top channel of all ALoCs. After detaching the cells from the T75 flasks,
354 they were adjusted to a concentration of 1 x 10^6 cells/mL in SAGM medium described above. The
355 bottom channels were filled with SAGM medium during epithelial cell seeding. 50 μL of the AT cell
356 suspension was pipetted into the top channel rapidly and checked under a microscope to ensure
357 correct seeding density and cell homogeneity. Of note, the top channel volume is ~28 μL total,
358 but to ensure no bubbles are introduced, the channels are overfilled and the flow-through gently
359 aspirated. Once all chips were seeded, they were placed in a chip cradle (Emulate) and incubated
360 at 37°C for at least 2 hours. After confirming all cells had attached, each top and bottom channel
361 were gently washed with 200 μL of warm SAGM medium and incubated overnight at 37°C.
362 HMVECs were seeded 2-3 days later in the bottom channels of all ALoCs. Prior to HMVEC cell
363 seeding, media was replenished daily for the ATs seeded on the ALoCs. The SAGM medium used
364 for maintenance of the ATs on the chips (hereby called AT Maintenance Medium) was
365 supplemented with Dexamethasone at 100 nM (Sigma D4902), Keratinocyte growth factor (KGF)
366 at 5 ng/mL (Thermo Fisher PHG0094), 8-Br-cAMP at 50 μM (Sigma B7880), and Isobutyl
367 methylxanthine (IBMX) at 25 μM (Sigma I7018). When HMVECs reached ~80% confluency, they
368 were detached and adjusted to a concentration of 5 x 10^6 cells/mL in EGM-2MV medium

369 (described above). The bottom channels of all ALoCs were filled with EGM-2MV medium prior to
370 seeding. 20 µL of the HMVEC cell suspension was pipetted rapidly into the bottom channel and
371 checked under the microscope for correct seeding density and cell homogeneity. The bottom
372 channel volume is ~6 µL total. Similarly to the top channel, the bottom channel was overfilled to
373 prevent the introduction of bubbles to the channel. The chip was then immediately flipped upside
374 down and placed in the chip cradle to ensure cells were seeded on the porous membrane in the
375 bottom channel. Once all ALoCs were seeded and flipped upside down, they were incubated at
376 37°C for at least 2 hours until all cells were attached. After all cells had attached, the bottom
377 channel was washed with 200 µL of warm EGM-2MV medium and incubated overnight at 37°C.

378 Prior to attaching ALoCs to Pods, warm EGM-2MV and AT Maintenance medium were degassed
379 using a Steriflip device for 5 min each to prevent air bubbles being trapped in the microfluidic lines
380 of the Pod. 3 mL of each medium were pipetted into its respective reservoir within the Pod. Using
381 Emulate's Zoe, the Pods were primed with medium to prevent bubbles from impeding medium
382 flow to the ALoCs. Once primed, each ALoC was snapped into each respective Pod. To further
383 help prevent bubble formation within the microfluidic lines, a Regulate Cycle was performed on
384 each chip via the Zoe. The ALoCs from this point on were harbored within the Pods and fresh
385 medium was exchanged through the chip at a flow rate of 30 µL/hr supplied by the Zoe.

386 After 24 hours of continuous media flow on all ALoCs, air-liquid interface (ALI) was introduced to
387 all ALoCs by removing all medium from the top channel and changing the top channel from liquid
388 media flow to air. The bottom channel medium was changed to ALI medium which comprised of
389 a Medium 199 base (Thermo Fisher 11043023) supplemented with 10 ng/mL Human Epidermal
390 Growth Factor (Peprotech AF-100-15), 3 ng/mL Human Basic Fibroblast Growth Factor
391 (Peprotech AF-100-18B), 0.125 ng/mL Human Vascular Endothelial Growth Factor (Peprotech
392 AF-100-20), 1 µg/mL Hydrocortisone (Sigma H0135), 10 µg/mL Heparin (Sigma H3149), 80 µM
393 di-butyryl cAMP (Sigma B7880), 1mM L-Glutamax (Gibco 35050-061), 20 nM Dexamethasone

394 (Sigma D4902), 1% Pen-Srep solution (Gibco 125140-122), and 2% FBS. Bottom channel liquid
395 flow rate was set to 30 µL/hr and fresh ALI medium was replenished in the bottom channel
396 reservoir every 2-3 days. After 48 hours of ALI, mechanical stretch (5%, 0.20 Hz) was initiated
397 using the Zoe. All ALoCs were maintained in this way until seeding of macrophages and infection
398 with *M. fortuitum*.

399 **Macrophage Seeding on ALoCs**

400 After 7 days of differentiation with M-CSF to HMDMs, macrophages were detached from petri
401 dishes using ice-cold 5 mM EDTA in PBS and gentle scraping. HMDMs were centrifuged at 300xg
402 for 5 min and resuspended in a 1:1 ratio of AT Maintenance Medium (without dexamethasone)
403 and Macrophage Medium to a concentration of 1 x 10^6 cells/mL. ALoCs were removed from the
404 Zoe and detached from the Pods, and top channel was washed with 200 µL of HPAEC
405 Maintenance Medium. With medium still in the top channel, 50 µL of HMDM cell suspension was
406 rapidly pipetted through the top channel. ALoCs were placed in square petri dishes and incubated
407 at 37°C with 5% CO_2 for 3-4 hours to allow attachment to the top channel. Once attached, ALoCs
408 were attached back to Pods after priming and after 2 hours of a Regulate Cycle were returned to
409 ALI.

410 ***M. fortuitum* Infection on Human ALoC**

411 Upon returning ALoCs to ALI conditions after macrophage attachment to the ALoCs, ALI medium
412 was replaced with ALI medium without penicillin/streptomycin, to avoid impacting subsequent
413 bacterial infection. Twenty-four hours after returning to ALI conditions, the ALoCs were infected
414 with *M. fortuitum*. mCherry-expressing *M. fortuitum* was cultured at 37°C in liquid 7H9 medium
415 (BD Difco 271310) supplemented with 10% OADC enrichment (BD 212351), 50 µg/mL
416 Kanamycin (Sigma 60615) and 0.05% Tyloxapol (Sigma T8761) until it reached an OD_{600} 0.5 –
417 0.7. The culture was pelleted by centrifugation at 3500 RPM for 10 min. The pellet was washed

418 three times with 50 mL of 1X PBS (-Ca^+/-Mg^+) by centrifugation at 3500 RPM for 10 min, and
419 resuspended in 5 mL PBS for a slow spin to remove cell debris at 500 RPM for 5 min. The
420 supernatant was collected and passed through a 26-gauge needle three times to generate a
421 single-cell suspension. The bacterial suspension was adjusted to an MOI of 1 with respect to the
422 epithelial cells in HPAEC Maintenance Medium, and 50 µL of the *M. fortuitum* suspension was
423 pipetted rapidly through the top channel. The ALoCs were incubated at 37°C for 1 hr. under static
424 conditions, and then washed three times with epithelial medium before returning ALoCs back to
425 Pods and into the Zoe for another Regulate Cycle. ALI was initiated again and the ALoCs were
426 infected for a total of 24 hours.

427 **RNA Extraction from ALoCs**

428 ALoCs were removed from the Zoe and Pods. Top and bottom channels were washed three times
429 with 200 µL of ice-cold 1X DPBS (-Ca^+/-Mg^+). An empty p200 filtered tip was inserted into the
430 bottom inlet, bottom outlet, and top outlet ports. 200 µL of TRIzol reagent (Invitrogen #15596026)
431 was pipetted in each ALoC by rapidly pressing and releasing the plunger three times before
432 collecting the supernatant in an RNase-free 1.5 mL tube. This process was repeated once more
433 for a total of ~400 µL of supernatant. TRIzol was added to each tube of RNA to a final volume of
434 1 mL. The RNA was stored at -80°C before extraction using the Qiagen RNeasy Mini Columns
435 (74106). AT and macrophage lysates were thawed on ice and incubated at room temperature for
436 5 min. 200 µL of chloroform per 1 mL of lysates was added to each tube, shaken vigorously for
437 15 sec., incubated at room temperature for 2-3 min, and centrifuged for 5 min at 12,000xg at 4°C.
438 The aqueous phase was transferred to fresh RNase-free tubes and the rest of the RNA extraction
439 was performed according to the Qiagen RNeasy Mini Column Kit. Extracted RNA was stored at -
440 80°C until use for library preparation and RNA-sequencing.

441 **Library Preparation and RNA-sequencing**

442 Samples were analyzed on an Agilent Tapestation 4200 to determine level of degradation to
443 ensure that only high quality RNA was used (RIN Score 8 or higher). We used a Qubit 4.0
444 Fluorimeter (ThermoFisher) to determine RNA concentration prior to starting library prep. One
445 microgram of total DNAse treated RNA was then prepared with the TruSeq Stranded mRNA
446 Library Prep Kit (Illumina). Poly-A RNA was purified and fragmented before strand-specific cDNA
447 synthesis. cDNA was then A-tailed and indexed adapters ligated. After adapter ligation, samples
448 were PCR amplified and purified with AmpureXP beads, then validated again on the Agilent
449 Tapestation 4200. Before being normalized and pooled, samples were quantified by Qubit then
450 sequenced on the Illumina NextSeq 2000 using a P2-100 flowcell.

451 **Bulk RNA-sequencing Analysis**

452 All RNA-sequencing analyses were performed using integrated Differential Expression and
453 Pathways Analysis, iDEP 2.01 (Ge et al., 2018). Genes expressed at extremely low levels were
454 filtered out of the gene set by removing any genes with less than 0.4 counts per million (CPM) in
455 at least one sample (n=1) (**Supplemental Figure 3A**). 13,934 filtered genes were converted to
456 Ensembl gene IDs, normalized in edgeR and transformed via rlog. Hierarchical clustering of the
457 samples and the top 2000 genes were performed (**Supplemental Figure 3B**). We then performed
458 principal component analysis (PCA) using the 2000 most variable genes. Using DESeq2 and the
459 Wald test (FDR cutoff = 0.1, minimum fold change = 1.5), we generated adjusted p-values and
460 $\log_2$ fold changes. Gene expression was then compared between the “infected” AloCs and
461 “control_uninfected” ALoCs. A total of 1,454 genes were found to be downregulated ($\log_2$ fold
462 change <1) and 588 genes were upregulated ($\log_2$ fold change >1). Using analysis of variance
463 (ANOVA) and post-hoc pairwise t-tests, we evaluated between-group differences for each cluster
464 using these scaled expression values. We performed functional enrichment analysis using the
465 hypergeometric test in hypeR for enriched pathways within the differentially expressed gene set.
466 Enrichment analysis was run using significantly upregulated and significantly downregulated

467 genes. Gene categories with fewer than 15 genes were excluded. Gene categories were
468 considered significant if they had Benjamini-Hochberg adjusted *p*-values less than 0.1.

469 **Immunofluorescence**

470 ALoCs were washed three times with 200 µL of 1X DPBS and 200 uL of 4% PFA in PBS were
471 added to each channel of each ALoC for 20 min. at room temperature. ALoCs were washed three
472 times with 200 µL of 1X DPBS and incubated for 30 min. at room temperature with 200 µL of 0.1%
473 Triton X-100 and 2% saponin. The ALoCs were then washed three times with 200 µL of 1X DPBS
474 and incubated overnight at 4°C with primary antibody (1:100) (**Supplemental Table 1**). ALoCs
475 were washed again three times with 200 µL of DPBS and incubated with secondary antibody
476 (1:1000) (**Supplemental Table 1**) for 2 hours at room temperature, protected from light. ALoCs
477 were washed three times with 200 µL of 1X DPBS and incubated with DAPI for 10 min at room
478 temperature. They were washed again three times with 200 µL of 1X DPBS and stored at 4°C
479 with both channels filled with 1X DPBS. Confocal images were acquired on a Nikon CSU W1
480 spinning disk confocal microscope with an CFI S Plan Fluor ELWD 10X objective.

481 **Statistical analyses**

482 All statistical analyses were performed using GraphPad Prism Software (version 9). For *in vitro*
483 studies, data was analyzed using unpaired two-tailed *t*-test. For RNA sequencing analysis,
484 analysis of variance (ANOVA) and post-hoc pairwise t-tests were used to evaluate between-group
485 differences for each cluster using scaled expression values.

486 **ACKNOWLEDGEMENTS**

487 The authors thank Gautam Mahajan and Ben Swenor from Emulate Inc. for providing protocols
488 and support. The authors also thank core facilities at UT Southwestern Medical Center for their
489 important contributions to this work including the UT Southwestern McDermott Center Next
490 Generation Sequencing (NGS) Core and the Quantitative Light Microscopy Core, particularly the

core director Marcel Mettlen, a Shared Resource of the Harold C. Simmons Cancer Center, supported in part by an NCI Cancer Center Support Grant, 1P30 CA142543-01.

COMPETING INTERESTS

All authors declare that they have no competing interests.

FUNDING

This work was supported by the National Institutes of Health U19 AI142784, R01 AI184584, R01 AI158688 and P01 AI159402 to M.U.S.

DATA AVAILABILITY

Bulk RNA sequencing data has been deposited at the NCBI GEO database, GSE276053, and will be made publicly available at the time of publication.

AUTHOR CONTRIBUTIONS

Conceptualization, V.E., M.U.S.; Formal analysis, V.E., M.U.S.; Funding acquisition, M.U.S.; Investigation, V.E., B.R., P.C.; Project administration, M.U.S.; Supervision, M.U.S.; Visualization, M.U.S.; Writing – original draft, V.E., M.U.S.; Writing – review and editing, All authors.

References

ALKARNI, M., LIPMAN, M. and LOWE, D. M. 2023. The roles of neutrophils in non-tuberculous mycobacterial pulmonary disease. *Ann Clin Microbiol Antimicrob,* 22**,** 14.

ARDAIN, A., DOMINGO-GONZALEZ, R., DAS, S., KAZER, S. W., HOWARD, N. C., SINGH, A., AHMED, M., NHAMOYEBONDE, S., RANGEL-MORENO, J., OGONGO, P., LU, L., RAMSURAN, D., DE LA LUZ GARCIA-HERNANDEZ, M., T, K. U., DARBY, M., PARK, E., KARIM, F., MELOCCHI, L., MADANSEIN, R., DULLABH, K. J., DUNLAP, M., MARIN-AGUDELO, N., EBIHARA, T., NDUNG'U, T., KAUSHAL, D., PYM, A. S., KOLLS, J. K., STEYN, A., ZUNIGA, J., HORSNELL, W., YOKOYAMA, W. M., SHALEK, A. K., KLOVERPRIS, H. N., COLONNA, M., LESLIE, A. and KHADER, S. A. 2019. Group 3 innate lymphoid cells mediate early protective immunity against tuberculosis. *Nature,* 570**,** 528-532.

516 BAI, H., SI, L., JIANG, A., BELGUR, C., ZHAI, Y., PLEBANI, R., OH, C. Y., RODAS, M., PATIL,
517 A., NURANI, A., GILPIN, S. E., POWERS, R. K., GOYAL, G., PRANTIL-BAUN, R. and
518 INGBER, D. E. 2022. Mechanical control of innate immune responses against viral infection
519 revealed in a human lung alveolus chip. *Nat Commun,* 13**,** 1928.

520 BALDWIN, S. L., LARSEN, S. E., ORDWAY, D., CASSELL, G. and COLER, R. N. 2019. The
521 complexities and challenges of preventing and treating nontuberculous mycobacterial
522 diseases. *PLoS Negl Trop Dis,* 13**,** e0007083.

523 BENAM, K. H., DAUTH, S., HASSELL, B., HERLAND, A., JAIN, A., JANG, K. J., KARALIS, K.,
524 KIM, H. J., MACQUEEN, L., MAHMOODIAN, R., MUSAH, S., TORISAWA, Y. S., VAN DER
525 MEER, A. D., VILLENAVE, R., YADID, M., PARKER, K. K. and INGBER, D. E. 2015.
526 Engineered in vitro disease models. *Annu Rev Pathol,* 10**,** 195-262.

527 BENAM, K. H., VILLENAVE, R., LUCCHESI, C., VARONE, A., HUBEAU, C., LEE, H. H.,
528 ALVES, S. E., SALMON, M., FERRANTE, T. C., WEAVER, J. C., BAHINSKI, A., HAMILTON,
529 G. A. and INGBER, D. E. 2016. Small airway-on-a-chip enables analysis of human lung
530 inflammation and drug responses in vitro. *Nat Methods,* 13**,** 151-7.

531 BERRY, M. P., GRAHAM, C. M., MCNAB, F. W., XU, Z., BLOCH, S. A., ONI, T., WILKINSON, K.
532 A., BANCHEREAU, R., SKINNER, J., WILKINSON, R. J., QUINN, C., BLANKENSHIP, D.,
533 DHAWAN, R., CUSH, J. J., MEJIAS, A., RAMILO, O., KON, O. M., PASCUAL, V.,
534 BANCHEREAU, J., CHAUSSABEL, D. and O'GARRA, A. 2010. An interferon-inducible
535 neutrophil-driven blood transcriptional signature in human tuberculosis. *Nature,* 466**,** 973-7.

536 BETHENCOURT, M. A., NGUYEN, A. D. and FERRER, G. 2024. Lung Nontuberculous
537 Mycobacterial Infections. *StatPearls.* Treasure Island (FL).

538 BOHRER, A. C., CASTRO, E., HU, Z., QUEIROZ, A. T. L., TOCHENY, C. E., ASSMANN, M.,
539 SAKAI, S., NELSON, C., BAKER, P. J., MA, H., WANG, L., ZILU, W., DU BRUYN, E., RIOU,
540 C., KAUFFMAN, K. D., TUBERCULOSIS IMAGING, P., MOORE, I. N., DEL NONNO, F.,
541 PETRONE, L., GOLETTI, D., MARTINEAU, A. R., LOWE, D. M., CRONAN, M. R.,
542 WILKINSON, R. J., BARRY, C. E., VIA, L. E., BARBER, D. L., KLION, A. D., ANDRADE, B.
543 B., SONG, Y., WONG, K. W. and MAYER-BARBER, K. D. 2021. Eosinophils are part of the
544 granulocyte response in tuberculosis and promote host resistance in mice. *J Exp Med,* 218.

545 CAMPBELL, G. R. and SPECTOR, S. A. 2012. Vitamin D inhibits human immunodeficiency
546 virus type 1 and Mycobacterium tuberculosis infection in macrophages through the induction
547 of autophagy. *PLoS Pathog,* 8**,** e1002689.

548 CAVERLY, L. J., CACERES, S. M., FRATELLI, C., HAPPOLDT, C., KIDWELL, K. M.,
549 MALCOLM, K. C., NICK, J. A. and NICHOLS, D. P. 2015. Mycobacterium abscessus
550 morphotype comparison in a murine model. *PLoS One,* 10**,** e0117657.

551 CHAN, E. D., BAI, X., ORDWAY, D. J. and VERMA, D. 2016. Animal Models of Non-
552 Tuberculous Mycobacterial Infections. *Mycobacterial Diseases,* 6.

553 COWMAN, S. A., JACOB, J., HANSELL, D. M., KELLEHER, P., WILSON, R., COOKSON, W.
554 O. C., MOFFATT, M. F. and LOEBINGER, M. R. 2018. Whole-Blood Gene Expression in
555 Pulmonary Nontuberculous Mycobacterial Infection. *Am J Respir Cell Mol Biol,* 58**,** 510-518.

556 CRISTANCHO-ROJAS, C., VARLEY, C. D., LARA, S. C., KHERABI, Y., HENKLE, E. and
557 WINTHROP, K. L. 2023. Epidemiology of Mycobacterium abscessus. *Clin Microbiol Infect*.

558 DASGUPTA, Q., JIANG, A., WEN, A. M., MANNIX, R. J., MAN, Y., HALL, S., JAVORSKY, E.
559 and INGBER, D. E. 2023. A human lung alveolus-on-a-chip model of acute radiation-induced
560 lung injury. *Nat Commun,* 14**,** 6506.

561 DE GROOTE, M. A., JOHNSON, L., PODELL, B., BROOKS, E., BASARABA, R. and
562 GONZALEZ-JUARRERO, M. 2014. GM-CSF knockout mice for preclinical testing of agents
563 with antimicrobial activity against Mycobacterium abscessus. *J Antimicrob Chemother,* 69**,**
564 1057-64.

565 DEINHARDT-EMMER, S., RENNERT, K., SCHICKE, E., CSERESNYES, Z., WINDOLPH, M.,
566 NIETZSCHE, S., HELLER, R., SIWCZAK, F., HAUPT, K. F., CARLSTEDT, S., SCHACKE, M.,
567 FIGGE, M. T., EHRHARDT, C., LOFFLER, B. and MOSIG, A. S. 2020. Co-infection with
568 Staphylococcus aureus after primary influenza virus infection leads to damage of the
569 endothelium in a human alveolus-on-a-chip model. *Biofabrication,* 12**,** 025012.

570 DONOHUE, M. J. 2021. Epidemiological risk factors and the geographical distribution of eight
571 Mycobacterium species. *BMC Infect Dis,* 21**,** 258.

572 FRANCO, L. H., NAIR, V. R., SCHARN, C. R., XAVIER, R. J., TORREALBA, J. R., SHILOH, M.
573 U. and LEVINE, B. 2017. The Ubiquitin Ligase Smurf1 Functions in Selective Autophagy of
574 Mycobacterium tuberculosis and Anti-tuberculous Host Defense. *Cell Host Microbe,* 21**,** 59-
575 72.

576 FU, Y. L. and HARRISON, R. E. 2021. Microbial Phagocytic Receptors and Their Potential
577 Involvement in Cytokine Induction in Macrophages. *Front Immunol,* 12**,** 662063.

578 GANGADHARAM, P. R. 1995. Beige mouse model for Mycobacterium avium complex disease.
579 *Antimicrob Agents Chemother,* 39**,** 1647-54.

580 GE, S. X., SON, E. W. and YAO, R. 2018. iDEP: an integrated web application for differential
581 expression and pathway analysis of RNA-Seq data. *BMC Bioinformatics,* 19**,** 534.

582 GONZALEZ-PEREZ, M., MARINO-RAMIREZ, L., PARRA-LOPEZ, C. A., MURCIA, M. I.,
583 MARQUINA, B., MATA-ESPINOZA, D., RODRIGUEZ-MIGUEZ, Y., BAAY-GUZMAN, G. J.,
584 HUERTA-YEPEZ, S. and HERNANDEZ-PANDO, R. 2013. Virulence and immune response
585 induced by Mycobacterium avium complex strains in a model of progressive pulmonary
586 tuberculosis and subcutaneous infection in BALB/c mice. *Infect Immun,* 81**,** 4001-12.

587 HAIQING BAI, L. S., AMANDA JIANG, CHAITRA BELGUR, YUNHAO ZHAI, ROBERTO
588 PLEBANI,, CRYSTAL YURI OH, M. R., ADITYA PATIL, ATIQ NURANI , SARAH E. GILPIN,
589 RANI K. POWERS, GIRIJA GOYAL, and INGBER, R. P.-B. D. E. 2022. Mechanical control of
590 innate immune responses against viral infection revealed in a human lung alveolus chip.
591 *Nature Communications,* 13.

592 HOANG, T. N. M., CSERESNYES, Z., HARTUNG, S., BLICKENSDORF, M., SAFFER, C.,
593 RENNERT, K., MOSIG, A. S., VON LILIENFELD-TOAL, M. and FIGGE, M. T. 2022. Invasive
594 aspergillosis-on-chip: A quantitative treatment study of human Aspergillus fumigatus infection.
595 *Biomaterials,* 283**,** 121420.

596 HUH, D., LESLIE, D. C., MATTHEWS, B. D., FRASER, J. P., JUREK, S., HAMILTON, G. A.,
597 THORNELOE, K. S., MCALEXANDER, M. A. and INGBER, D. E. 2012a. A human disease
598 model of drug toxicity-induced pulmonary edema in a lung-on-a-chip microdevice. *Sci Transl*
599 *Med,* 4**,** 159ra147.

600 HUH, D., MATTHEWS, B. D., MAMMOTO, A., MONTOYA-ZAVALA, M., HSIN, H. Y. and
601 INGBER, D. E. 2010. Reconstituting organ-level lung functions on a chip. *Science,* 328**,**
602 1662-8.

603 HUH, D., TORISAWA, Y. S., HAMILTON, G. A., KIM, H. J. and INGBER, D. E. 2012b.
604 Microengineered physiological biomimicry: organs-on-chips. *Lab Chip,* 12**,** 2156-64.

605 JAIN, A., BARRILE, R., VAN DER MEER, A. D., MAMMOTO, A., MAMMOTO, T., DE
606 CEUNYNCK, K., AISIKU, O., OTIENO, M. A., LOUDEN, C. S., HAMILTON, G. A.,
607 FLAUMENHAFT, R. and INGBER, D. E. 2018. Primary Human Lung Alveolus-on-a-chip
608 Model of Intravascular Thrombosis for Assessment of Therapeutics. *Clin Pharmacol Ther,*
609 103**,** 332-340.

610 JOHANSEN, M. D. and KREMER, L. 2020. CFTR Depletion Confers Hypersusceptibility to
611 Mycobacterium fortuitum in a Zebrafish Model. *Front Cell Infect Microbiol,* 10**,** 357.

612 KILINC, G., WALBURG, K. V., FRANKEN, K., VALKENBURG, M. L., AUBRY, A., HAKS, M. C.,
613 SARIS, A. and OTTENHOFF, T. H. M. 2022. Development of Human Cell-Based In Vitro
614 Infection Models to Determine the Intracellular Survival of Mycobacterium avium. *Front Cell*
615 *Infect Microbiol,* 12**,** 872361.

616 KIM, S. R., YU, J. Y., KIM, S. Y., KIM, D. H. and JHUN, B. W. 2023. Clinical Characteristics and
617 Treatment Outcomes of Mycobacterium fortuitum Pulmonary Disease. *Microbiol Spectr,* 11**,**
618 e0205123.

619 KIMMEY, J. M., HUYNH, J. P., WEISS, L. A., PARK, S., KAMBAL, A., DEBNATH, J., VIRGIN, H.
620 W. and STALLINGS, C. L. 2015. Unique role for ATG5 in neutrophil-mediated
621 immunopathology during M. tuberculosis infection. *Nature,* 528**,** 565-9.

622 KLEVER, A. M., ALEXANDER, K. A., ALMEIDA, D., ANDERSON, M. Z., BALL, R. L., BEAMER,
623 G., BOGGIATTO, P., BUIKSTRA, J. E., CHANDLER, B., CLAEYS, T. A., CONCHA, A. E.,
624 CONVERSE, P. J., DERBYSHIRE, K. M., DOBOS, K. M., DUPNIK, K. M., ENDSLEY, J. J.,
625 ENDSLEY, M. A., FENNELLY, K., FRANCO-PAREDES, C., HAGGE, D. A., HALL-
626 STOODLEY, L., HAYES, D., JR., HIRSCHFELD, K., HOFMAN, C. A., HONDA, J. R., HULL,
627 N. M., KRAMNIK, I., LACOURCIERE, K., LAHIRI, R., LAMONT, E. A., LARSEN, M. H.,
628 LEMAIRE, T., LESELLIER, S., LEE, N. R., LOWRY, C. A., MAHFOOZ, N. S., MCMICHAEL,
629 T. M., MERLING, M. R., MILLER, M. A., NAGAJYOTHI, J. F., NELSON, E.,
630 NUERMBERGER, E. L., PENA, M. T., PEREA, C., PODELL, B. K., PYLE, C. J., QUINN, F.
631 D., RAJARAM, M. V. S., MEJIA, O. R., ROTHOFF, M., SAGO, S. A., SALVADOR, L. C. M.,
632 SIMONSON, A. W., SPENCER, J. S., SREEVATSAN, S., SUBBIAN, S., SUNSTRUM, J.,
633 TOBIN, D. M., VIJAYAN, K. K. V., WRIGHT, C. T. O. and ROBINSON, R. T. 2023. The Many
634 Hosts of Mycobacteria 9 (MHM9): A conference report. *Tuberculosis (Edinb),* 142**,** 102377.

635 KREMER, M. D. J. A. L. 2020. CFTR Depletion Confers Hypersusceptibility to Mycobacterium
636 fortuitum in a Zebrafish Model. *Frontiers in Cellular and Infection Microbiology,* 10.

637 LAGUNE, M., KREMER, L. and HERRMANN, J. L. 2023. Mycobacterium abscessus, a complex
638 of three fast-growing subspecies sharing virulence traits with slow-growing mycobacteria.
639 *Clin Microbiol Infect*.

640 LI, J., WANG, Z., CHU, Q., JIANG, K., LI, J. and TANG, N. 2018. The Strength of Mechanical
641 Forces Determines the Differentiation of Alveolar Epithelial Cells. *Dev Cell,* 44**,** 297-312 e5.

642 LI, J., WEN, A. M., POTLA, R., BENSHIRIM, E., SEEBARRAN, A., BENZ, M. A., HENRY, O. Y.
643 F., MATTHEWS, B. D., PRANTIL-BAUN, R., GILPIN, S. E., LEVY, O. and INGBER, D. E.
644 2019. AAV-mediated gene therapy targeting TRPV4 mechanotransduction for inhibition of
645 pulmonary vascular leakage. *APL Bioeng,* 3**,** 046103.

646 LINDESTAM ARLEHAMN, C. S., BENSON, B., KUAN, R., DILL-MCFARLAND, K. A.,
647 PETERSON, G. J., PAUL, S., NGUYEN, F. K., GILMAN, R. H., SAITO, M., TAPLITZ, R.,
648 ARENTZ, M., GOSS, C. H., AITKEN, M. L., HORNE, D. J., SHAH, J. A., SETTE, A. and
649 HAWN, T. R. 2022. T-cell deficiency and hyperinflammatory monocyte responses associate
650 with Mycobacterium avium complex lung disease. *Front Immunol,* 13**,** 1016038.

651 LUKE, C. J., MARKOVINA, S., GOOD, M., WIGHT, I. E., THOMAS, B. J., LINNEMAN, J. M.,
652 LANIK, W. E., KOROLEVA, O., COFFMAN, M. R., MIEDEL, M. T., GONG, Q., ANDRESS, A.,
653 CAMPOS GUERRERO, M., WANG, S., CHEN, L., BEATTY, W. L., HAUSMANN, K. N.,
654 WHITE, F. V., FITZPATRICK, J. A. J., ORVEDAHL, A., PAK, S. C. and SILVERMAN, G. A.
655 2022. Lysoptosis is an evolutionarily conserved cell death pathway moderated by intracellular
656 serpins. *Commun Biol,* 5**,** 47.

657 MERCALDO, R. A., MARSHALL, J. E., CANGELOSI, G. A., DONOHUE, M., FALKINHAM, J.
658 O., 3RD, FIERER, N., FRENCH, J. P., GEBERT, M. J., HONDA, J. R., LIPNER, E. M.,
659 MARRAS, T. K., MORIMOTO, K., SALFINGER, M., STOUT, J., THOMSON, R. and
660 PREVOTS, D. R. 2023. Environmental risk of nontuberculous mycobacterial infection:
661 Strategies for advancing methodology. *Tuberculosis (Edinb),* 139**,** 102305.

662 MISHRA, R., HANNEBELLE, M., PATIL, V. P., DUBOIS, A., GARCIA-MOUTON, C., KIRSCH, G.
663 M., JAN, M., SHARMA, K., GUEX, N., SORDET-DESSIMOZ, J., PEREZ-GIL, J., PRAKASH,
664 M., KNOTT, G. W., DHAR, N., MCKINNEY, J. D. and THACKER, V. V. 2023.
665 Mechanopathology of biofilm-like Mycobacterium tuberculosis cords. *Cell,* 186**,** 5135-5150
666 e28.

667 NOBS, E., LASCHANZKY, K., MUNKE, K., MOVERT, E., VALFRIDSSON, C. and CARLSSON,
668 F. 2024. Cytosolic serpins act in a cytoprotective feedback loop that limits ESX-1-dependent
669 death of Mycobacterium marinum-infected macrophages. *mBio***,** e0038424.

670 ORDWAY, D., HENAO-TAMAYO, M., SMITH, E., SHANLEY, C., HARTON, M., TROUDT, J.,
671 BAI, X., BASARABA, R. J., ORME, I. M. and CHAN, E. D. 2008. Animal model of
672 Mycobacterium abscessus lung infection. *J Leukoc Biol,* 83**,** 1502-11.

673 ORME, I. M. and ORDWAY, D. J. 2014. Host response to nontuberculous mycobacterial
674 infections of current clinical importance. *Infect Immun,* 82**,** 3516-22.

675 QIN, M. H., MADIRAJU, M. V. and RAJAGOPALAN, M. 1999. Characterization of the functional
676 replication origin of Mycobacterium tuberculosis. *Gene,* 233**,** 121-30.

677 RAMPACCI, E., STEFANETTI, V., PASSAMONTI, F. and HENAO-TAMAYO, M. 2020.
678 Preclinical Models of Nontuberculous Mycobacteria Infection for Early Drug Discovery and
679 Vaccine Research. *Pathogens,* 9.

680 ROQUET-BANERES, F., ALCARAZ, M., HAMELA, C., ABENDROTH, J., EDWARDS, T. E. and
681 KREMER, L. 2023. In Vitro and In Vivo Efficacy of NITD-916 against Mycobacterium
682 fortuitum. *Antimicrob Agents Chemother,* 67**,** e0160722.

683 TABONE, O., VERMA, R., SINGHANIA, A., CHAKRAVARTY, P., BRANCHETT, W. J., GRAHAM,
684 C. M., LEE, J., TRANG, T., REYNIER, F., LEISSNER, P., KAISER, K., RODRIGUE, M.,

WOLTMANN, G., HALDAR, P. and O'GARRA, A. 2021. Blood transcriptomics reveal the evolution and resolution of the immune response in tuberculosis. *J Exp Med,* 218.

THACKER, V. V., DHAR, N., SHARMA, K., BARRILE, R., KARALIS, K. and MCKINNEY, J. D. 2020. A lung-on-chip model of early Mycobacterium tuberculosis infection reveals an essential role for alveolar epithelial cells in controlling bacterial growth. *Elife,* 9.

TOURE, H., GALINDO, L. A., LAGUNE, M., GLATIGNY, S., WATERHOUSE, R. M., GUENAL, I., HERRMANN, J. L., GIRARD-MISGUICH, F. and SZUPLEWSKI, S. 2023. Mycobacterium abscessus resists the innate cellular response by surviving cell lysis of infected phagocytes. *PLoS Pathog,* 19**,** e1011257.

VARLEY, C. D. and WINTHROP, K. L. 2022. Nontuberculous Mycobacteria: Diagnosis and Therapy. *Clin Chest Med,* 43**,** 89-98.

WANG, L., MA, H., WEN, Z., NIU, L., CHEN, X., LIU, H., ZHANG, S., XU, J., ZHU, Y., LI, H., CHEN, H., SHI, L., WAN, L., LI, L., LI, M., WONG, K. W. and SONG, Y. 2023a. Single-cell RNA-sequencing reveals heterogeneity and intercellular crosstalk in human tuberculosis lung. *J Infect,* 87**,** 373-384.

WANG, L., ZHENG, X., MA, J., GU, J. and SHA, W. 2023b. Comparative Proteomic Analysis of Exosomes Derived from Patients Infected with Non-Tuberculous Mycobacterium and Mycobacterium tuberculosis. *Microorganisms,* 11.

WANG, P., YANG, G. L., HE, Y. F., SHEN, Y. H., HAO, X. H., LIU, H. P., SHEN, H. B., WANG, L. and SHA, W. 2024. Single-cell transcriptomics of blood identified IFIT1(+) neutrophil subcluster expansion in NTM-PD patients. *Int Immunopharmacol,* 137**,** 112412.

WINTHROP, K. L., MARRAS, T. K., ADJEMIAN, J., ZHANG, H., WANG, P. and ZHANG, Q. 2020. Incidence and Prevalence of Nontuberculous Mycobacterial Lung Disease in a Large U.S. Managed Care Health Plan, 2008-2015. *Ann Am Thorac Soc,* 17**,** 178-185.

710 **Figure legends**

711 **Figure 1**. **Establishment of a fully humanized alveolus lung-on-a-chip (ALoC) model system**
712 **A.** Schematic of a human alveolus and the surrounding vasculature, highlighting alveolar epithelial
713 type I (ATI), alveolar epithelial type II (AT2) cells, and alveolar macrophages in the alveolar sac,
714 with pulmonary microvascular endothelial cells lining the vasculature. **B.** Cross-section of the
715 ALoC model for *M. fortuitum* infection. The apical channel contains primary human alveolar
716 epithelial cells (ATI and ATII) with or without human $CD14^+$ peripheral blood-derived
717 macrophages, while the basal channel is lined by human primary pulmonary microvascular
718 endothelial cells (HMVECs). **C.** Schematic of the addition of macrophages to the apical channel.
719 **D.** Stitched image of the apical channel of the ALoC at 15 days of culture highlighting AT1 cells
720 ($HT1^+$, red) and AT2 cells ($HT2^+$, green). Nuclei are labelled with DAPI (blue). Scale bar = 1000
721 µm. **E.** Epifluorescent image of differentiated AT1 and AT2 cells on the ALoC. Scale bar = 200
722 µm. **F.** Three-dimensional immunofluorescence reconstruction of ALoC after 15 days of culture,
723 highlighting differentiated AT2 cells and AT1 cells. Scale bar = 500 µm**.** **G.** Cross-sectional image
724 of the ALoC highlighting AT1 and AT2 cells in a monolayer. Scale bar = 200 µm**.** **H.** Stitched
725 image of the apical epithelial channel of the ALoC after the addition of HMDMs ($CD14^+$, yellow)
726 on the ALoC. Nuclei are labelled with DAPI. Scale bar = 1,000 µm**.** **I.** Magnified view of the
727 outlined area in panel H of AT1 cells, AT2 cells, and macrophages. Scale bar = 200 µm**.** **J.** Three-
728 dimensional reconstruction of ALoC highlighting the addition of macrophages amongst
729 differentiated AT1 and AT2 cells. Scale bar = 200 µm**.** **K.** Cross-sectional image of the ALoC
730 showing AT1 cells ($HT1^+$, red), AT2 cells ($HT2^+$, green), and HMDMs ($CD14^+$, yellow). Scale bar
731 = 200 µm**.** Images are representative of at least 3 independent chips from 2 independent
732 experiments.

733 **Figure 2. *Mycobacterium fortuitum* infection on an Alveolus Lung-on-a-Chip without**
734 **macrophages A.** Schematic of *M. fortuitum* addition to the ALoC. *M. fortuitum* was added to the

735 ALoC at an MOI of 1 with respect to the alveolar epithelial cells. After 1 hour of static incubation
736 at 37°C, ALoCs were washed and returned to ALI. **B.** Stitched image of mCherry-expressing *M.*
737 *fortuitum* (red) on ALoCs with AT1 ($HT1^+$, purple) and AT2 ($HT2^+$, green) cells. Nuclei labelled with
738 DAPI (Blue). Scale bar = 500 μm**. C.** Immunofluorescence image highlighting alveolar epithelial
739 cell damage. Scale bar = 200 μm. **D.** Three-dimensional reconstruction of an infected ALoC
740 without macrophages. AT2 cells with "flattened" morphology highlighted within normal cuboidal
741 AT2 morphology. Scale bar = 200 μm**. E.** Cross-sectional image of *M. fortuitum* (mCherry, red)
742 infection on ALoC with AT1 and AT2 cells. Scale bar = 200 μm**.** Images are representative of at
743 least 3 independent chips from 2 independent experiments.

744 **Figure 3**. ***Mycobacterium fortuitum* infection on an Alveolus Lung-on-a-Chip containing**
745 **macrophages A.** Schematic of *M. fortuitum* infection on ALoC containing macrophages. 24 hours
746 after the addition macrophages, *M. fortuitum* was added to the ALoC at an MOI of 1 with respect
747 to the alveolar epithelial cells, incubated at 37°C for 1 hour, washed, and returned to ALI. **B**.
748 Stitched image of the apical channel, highlighting macrophages ($CD14^+$, grey) and AT2 cells
749 ($HT2^+$, green) 24 hours after infection with mCherry-expressing *M. fortuitum* (red). Nuclei are
750 labelled by DAPI. Scale bar = 500 μm. **C.** Immunofluorescence image highlighting *M. fortuitum*
751 (mCherry, red)-infected macrophages ($CD14^+$, grey) and AT2 cells ($HT2^+$, green). Scale bar = 200
752 μm. **D.** Three-dimensional reconstructed image of infected macrophages (CD14, grey) along the
753 edge of an ALoC. Scale bar = 350 μm. **E.** Cross-sectional image of *M. fortuitum* infection on ALoC
754 with the addition of macrophages. **F.** Three-dimensional reconstruction of *M. fortuitum* bacilli and
755 macrophages on ALoCs. Scale bar = 200 μm. **G.** Quantification of *M. fortuitum* bacilli within
756 macrophages or AT2 cell. Each point represents the cumulative number of *M. fortuitum* bacilli
757 counted in each cell type for 10 fields within a single chip (N=3 independent chips, $p<0.05$ by
758 unpaired Student's t-test). Images are representative of at least 3 independent chips from 2
759 independent experiments.

760 **Figure 4**. **Bulk RNA-seq Analysis of *M. fortuitum*-infected ALoCs with macrophages A.**
761 Heat-map of the top 2000 genes expressed in uninfected and *M. fortuitum*-infected ALoCs (24
762 hours post-infection) (N=3 per group) using Pearson distance and average linkage. **B.** The -$\log_{10}$
763 (Adjusted p-Value) was plotted against $\log_2$ fold change to create a volcano plot representing the
764 top 25 differentially expressed genes (DEGs). Genes with an adjusted p-value<25 and $\log_2$ fold
765 change<2 were filtered from this analysis. **C.** Heat map comparing the $\log_2$ fold change of the
766 most differentially expressed chemokines and cytokines in ALoCs infected with *M. fortuitum*
767 versus uninfected ALoCs after 24 hours of infection. **D.** Heat map comparing the $\log_2$ fold change
768 of the most differentially expressed SERPINs in ALoCS infected with *M. fortuitum* versus
769 uninfected ALoCs after 24 hours of infection.

770 **Supplemental Figure Legends**

771 **Supplemental Figure 1**. **Establishment of the Alveolus Lung-on-a-Chip Model**. **A.** Typical
772 timeline of a single alveolus lung-on-a-chip (ALoC) experiment. **B.** Three stitched images,
773 representative of the entire apical channel containing AT1 (HT1+, red) and AT2 cells (HT2+,
774 green). Nuclei are labeled with DAPI (blue). Scale bars = 500 μm. **C. left** Brightfield image of
775 ALoCs immediately after the addition human $CD14^+$ peripheral blood-derived macrophages
776 (macrophages) on top of the alveolar epithelial cells. **C. right** Brightfield image of ALoCs 24 hours
777 after the addition of macrophages. **D.** Stitched image of the entire apical channel of an ALoC
778 containing macrophages (CD14+), AT1 cells (HT1+), and AT2 cells (HT2+). Nuclei are labelled
779 DAPI (blue). Scalebar = 500 μm.

780 **Supplemental Figure 2**. **Alveolar epithelial type I and II co-staining on ALoCs infected with**
781 ***M. fortuitum***. **A.** Stitched image of an uninfected ALoC control containing AT1 (HT1+, red) and
782 AT2 (HT2+, green) cells. Nuclei are labelled with DAPI (blue). **B.** Confocal image of *M. fortuitum*-
783 infected ALoCs after 24 hours of infection, highlighting AT1 cells (HT1+, purple). Adherens
784 junctions are labelled with E-cadherin (yellow) and nuclei are labelled with DAPI. Scale bar = 500
785 μm. **C.** Confocal image highlighting AT2 cells (HT2+, green), adherens junctions (E-cadherin,
786 yellow) and nuclei (DAPI, blue). Scale bar = 500 μm. **D.** Confocal image showing the merged
787 channels of panels B and C, highlighting the co-staining of alveolar epithelial cells observed in *M.*
788 *fortuitum*-infected ALoCs after 24 hours of infection. Scale bar = 500 μm.

789 **Supplemental Figure 3**. **Bulk RNA-sequencing analysis of *M. fortuitum*-infected ALoCs A.**
790 Total raw read counts of uninfected (n=3) and *M. fortuitum*-infected (n=3) ALoCs. **B.** Pearson
791 (average linkage) clustering of *M. fortuitum*-infected ALoCs and uninfected ALoCs.

Figure 1

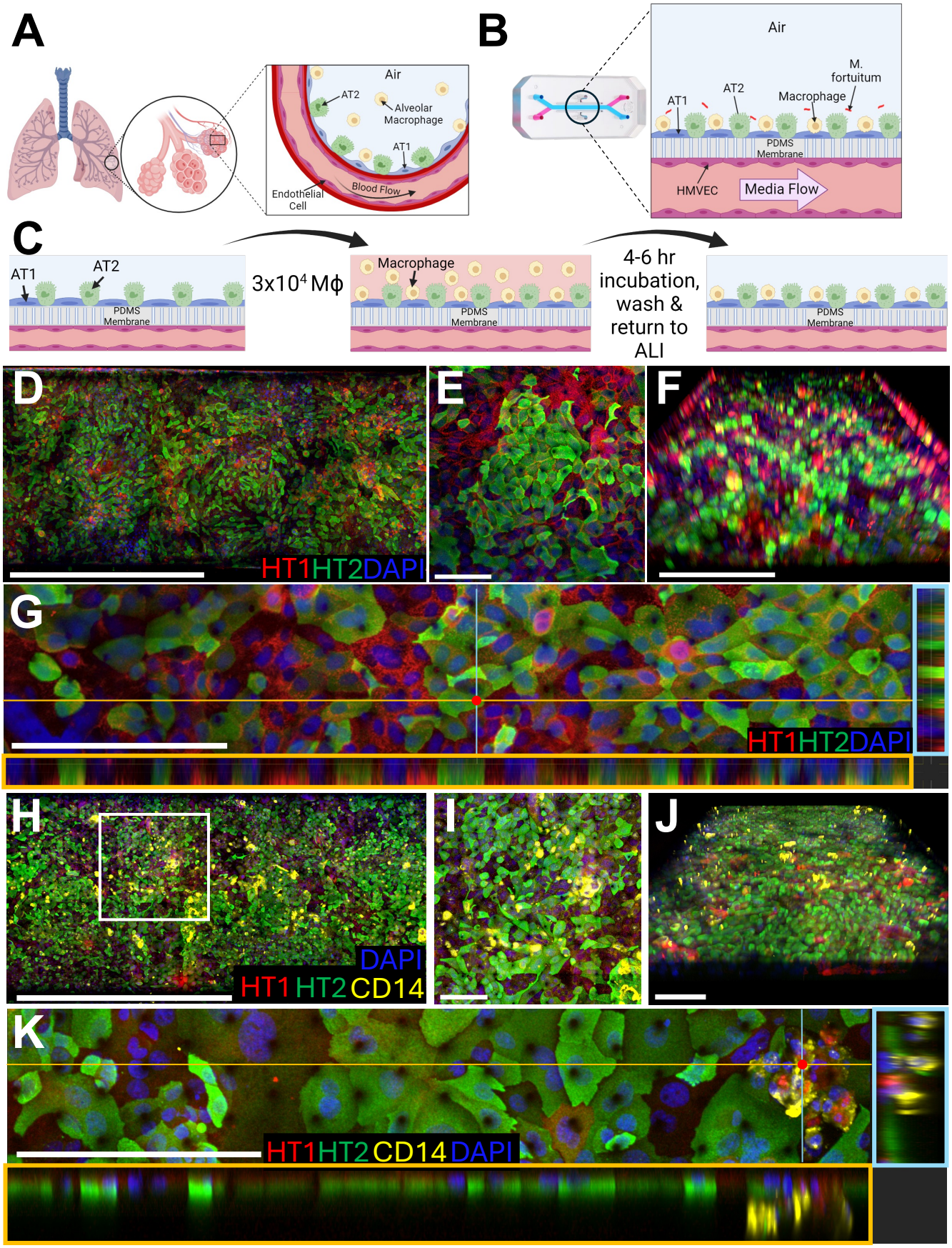
A
Air
AT2
Alveolar Macrophage
AT1
Endothelial Cell
Blood Flow
B
Air
M. fortuitum
AT1
AT2
Macrophage
PDMS Membrane
HMVEC
Media Flow
C
AT1
AT2
PDMS Membrane
3x10⁴ Mϕ
Macrophage
PDMS Membrane
4-6 hr incubation, wash & return to ALI
PDMS Membrane
D
HT1HT2DAPI
E
F
G
HT1HT2DAPI
H
DAPI
HT1 HT2 CD14
I
J
K
HT1HT2CD14DAPI

Figure 2

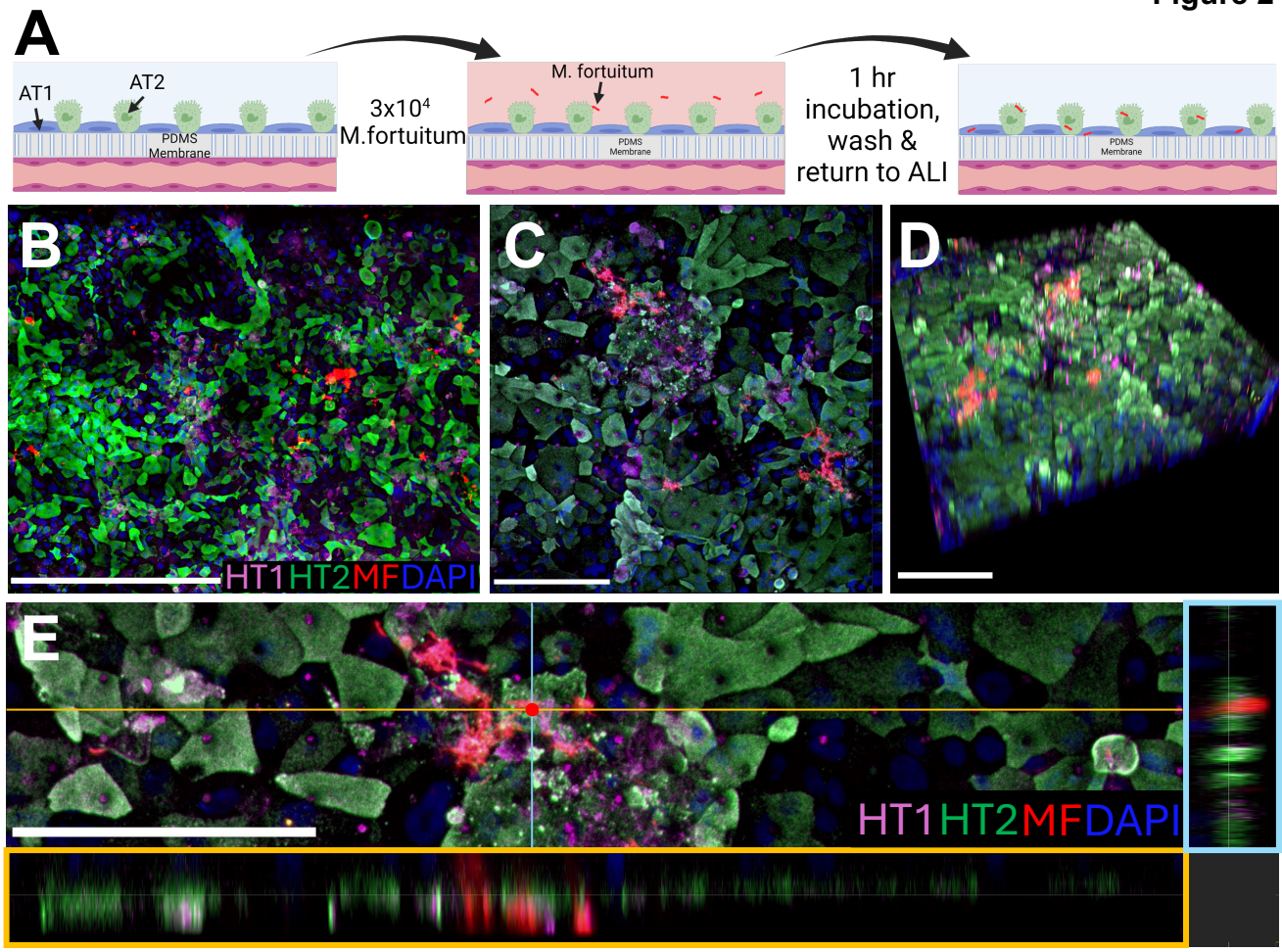
A
AT1
AT2
PDMS Membrane
3x10⁴ M.fortuitum
M. fortuitum
PDMS Membrane
1 hr incubation, wash & return to ALI
PDMS Membrane
B
HT1HT2MFDAPI
C
D
E
HT1HT2MFDAPI

Figure 3

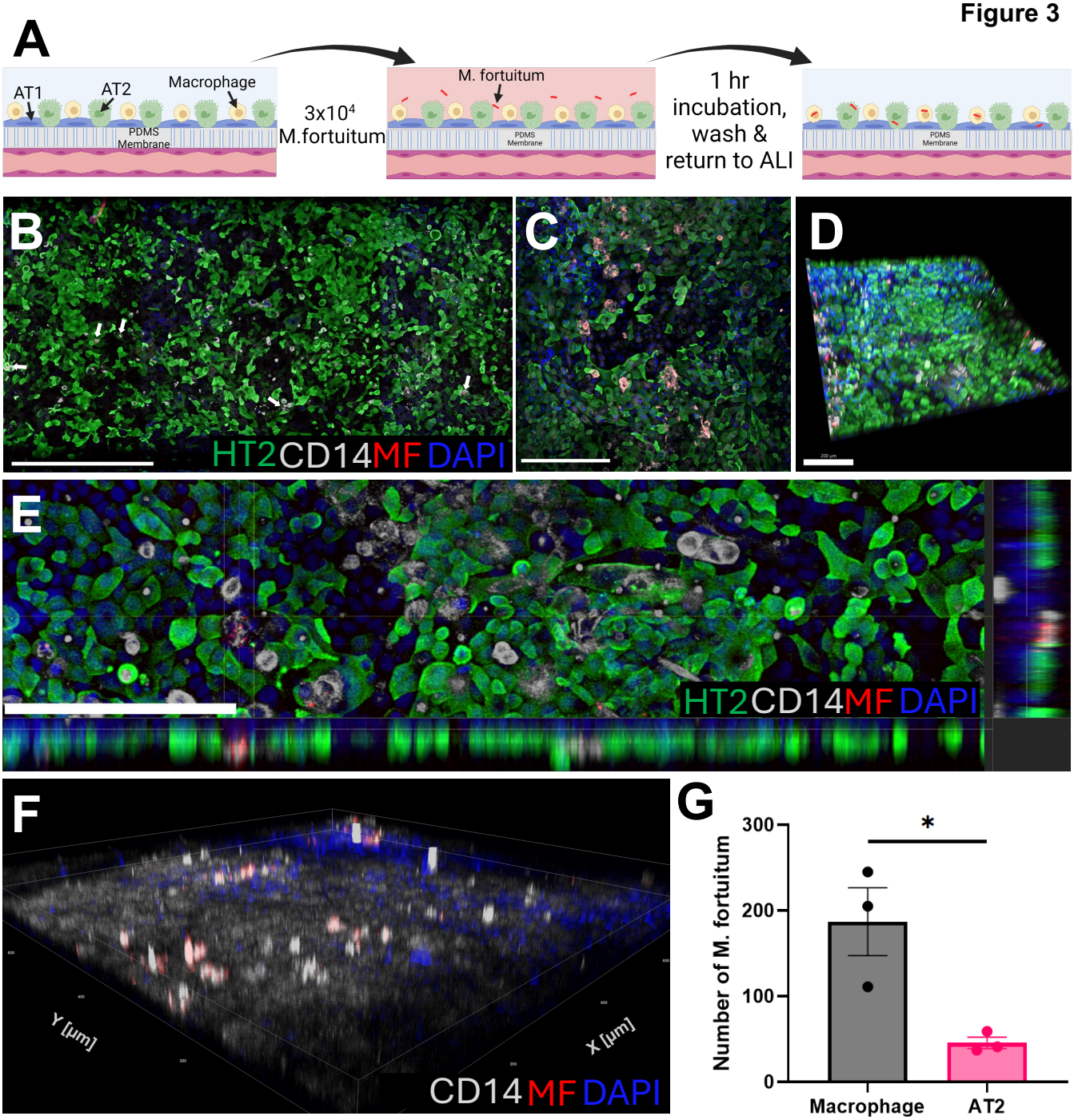
A
AT1
AT2
Macrophage
PDMS Membrane
3x10⁴ M.fortuitum
M. fortuitum
1 hr incubation, wash & return to ALI
B
HT2CD14MF DAPI
C
D
E
HT2CD14MF DAPI
F
Y [µm]
X [µm]
CD14MF DAPI
G
Number of M. fortuitum
300
200
100
0
*
Macrophage
AT2

Figure 4

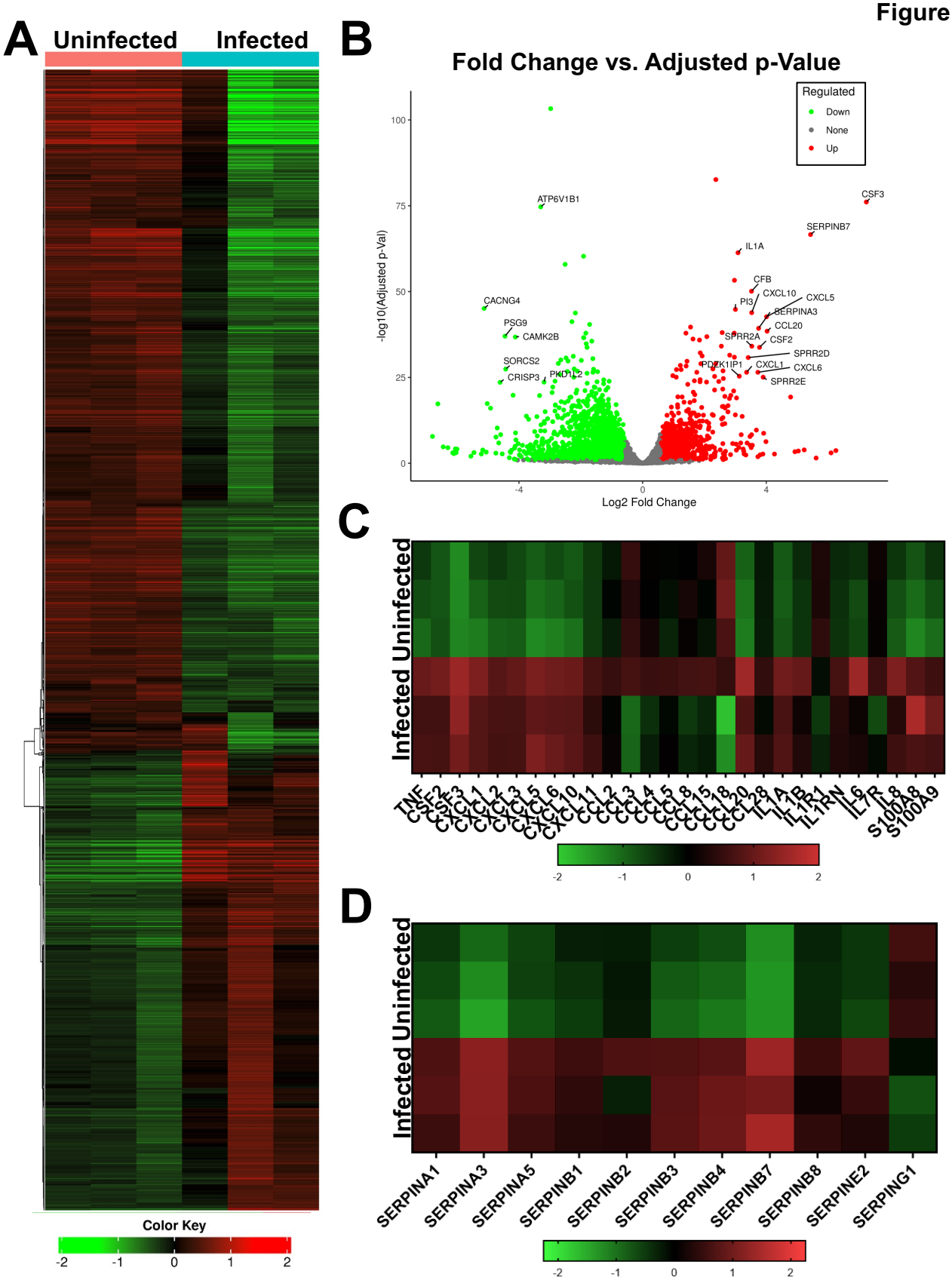
A
Uninfected
Infected
Color Key
-2
-1
0
1
2
B
Fold Change vs. Adjusted p-Value
Regulated
Down
None
Up
-log10(Adjusted p-Val)
Log2 Fold Change
ATP6V1B1
CACNG4
PSG9
CAMK2B
SORCS2
CRISP3
PKD1L2
CSF3
SERPINB7
IL1A
CFB
CXCL10
CXCL5
PI3
SERPINA3
CCL20
SPRR2A
CSF2
SPRR2D
PDZK1IP1
CXCL1
CXCL6
SPRR2E
C
Infected Uninfected
TNF
CSF2
CSF3
CXCL1
CXCL2
CXCL3
CXCL5
CXCL6
CXCL10
CCL1
CCL2
CCL3
CCL4
CCL5
CCL8
CCL15
CCL18
CCL20
CCL28
IL1A
IL1B
IL1R1
IL1RN
IL6
IL7R
IL8
S100A8
S100A9
D
Infected Uninfected
SERPINA1
SERPINA3
SERPINA5
SERPINB1
SERPINB2
SERPINB3
SERPINB4
SERPINB7
SERPINB8
SERPINE2
SERPING1

Table 1. The most significant up-regulated and down-regulated GO Biological Process pathways from M. fortuitum-infected ALoCs containing macrophages

Direction	GO Biological Process	Statistic	Genes	adj.Pval
Up	Response to bacterium	7.3996	438	1.1e-09
	Humoral immune response	6.5518	138	6.0e-07
	Defense response to bacterium	6.3097	169	1.1e-06
	Antimicrobial humoral response	6.0602	65	1.9e-05
	Response to molecule of bacterial origin	5.5061	251	3.7e-05
	Chemotaxis	5.2453	444	8.2e-05
	Taxis	5.2402	445	8.2e-05
	Response to lipopolysaccharide	5.2654	240	8.2e-05
	Antimicrobial humoral immune response mediated by antimicrobial peptide	5.6504	41	1.4e-04
Down	MRNA processing	-6.8939	402	4.4e-08
	RNA splicing	-6.5273	385	2.3e-07
	Histone modification	-5.7112	429	1.6e-05
	Proteasome-mediated ubiquitin-dependent protein catabolic process	-5.5755	410	2.5e-05
	Proteasomal protein catabolic process	-5.534	470	2.5e-05
	Chromatin organization	-5.4523	478	3.2e-05
	NcRNA metabolic process	-5.3774	477	4.2e-05
	Peptidyl-lysine modification	-5.128	343	1.5e-04
	RNA splicing via transesterification reactions with bulged adenosine as nucleophile	-5.1146	265	1.5e-04
	MRNA splicing via spliceosome	-5.1146	265	1.5e-04
	RNA splicing via transesterification reactions	-5.097	269	1.5e-04

Table 2. The most significant up-regulated and down-regulated GO Molecular Function pathways from M. fortuitum-infected ALoCs containing macrophages

Direction	GO Molecular Function	Statistic	Genes	adj.Pval
Up	Transmembrane signaling receptor activity	8.0205	486	1.9e-12
	Receptor ligand activity	6.4443	275	6.9e-08
	Signaling receptor regulator activity	6.3634	295	6.9e-08
	Signaling receptor activator activity	6.3463	281	6.9e-08
	Cytokine activity	5.657	148	4.8e-06
	Channel activity	5.1005	274	3.6e-05
	Passive transmembrane transporter activity	5.1005	274	3.6e-05
	Glycosaminoglycan binding	5.1296	151	3.7e-05
	Ion channel activity	4.8906	248	8.2e-05
	Calcium ion binding	4.8317	497	8.2e-05
	G protein-coupled receptor activity	4.872	193	8.3e-05
	Gated channel activity	4.7825	188	1.1e-04
	Extracellular matrix structural constituent	4.7767	119	1.3e-04
	Cation channel activity	4.7291	184	1.3e-04
	Inorganic molecular entity transmembrane transporter activity	4.6534	455	1.3e-04
	Heparin binding	4.4603	110	4.5e-04
	Endopeptidase regulator activity	4.3733	123	6.1e-04
	Inorganic cation transmembrane transporter activity	4.2753	363	6.3e-04
Down	Catalytic activity acting on RNA	-5.0214	311	3.8e-04
	Histone binding	-4.8025	216	6.4e-04

Supplemental Table 1. Antibodies used on ALoC for immunofluorescence

Cell Type	Target	Primary Antibody	Secondary Antibody
AT1	HT1	Anti HT1-56 (Terrace Biotech, TB-29AHT1-56)	Alpaca anti-Mouse IgG1 Nano (VHH) Recombinant Secondary Antibody conjugated with Alexa Fluor 647 (Thermo Fisher, SA5-10333)
AT1	PDPN	Anti-Podoplanin/gp36 antibody (18H5) (abcam, ab10288)	Alpaca anti-Mouse IgG1 Nano (VHH) Recombinant Secondary Antibody conjugated with Alexa Fluor 647 (Thermo Fisher, SA5-10333)
AT2	HT2	Anti HT2-280 (Terrace Biotech, TB-27AHT2-280)	Goat anti-Mouse IgG2a Cross-Adsorbed Secondary Antibody, Alexa Fluor 488 (Thermo Fisher, A21131)
Macrophage	CD14	CD14 Recombinant Rabbit Monoclonal Antibody (SC69-02) (Thermo Fisher, MA5-32248)	Donkey anti-Rabbit IgG (H+L), highly cross-adsorbed Secondary Antibody with Alexa Fluor 555 Plus
Epithelial cell	E-cadherin	E-Cadherin Recombinant Rabbit Monoclonal Antibody (5H6L18) (Invitrogen, 701134)	Donkey anti-Rabbit IgG (H+L), highly cross-adsorbed Secondary Antibody with Alexa Fluor 555 Plus
n/a	Nuclei	NucBlue™ Fixed Cell ReadyProbes™ Reagent (DAPI) (Thermo Fisher, R37606)	n/a

Supplemental Figure 1

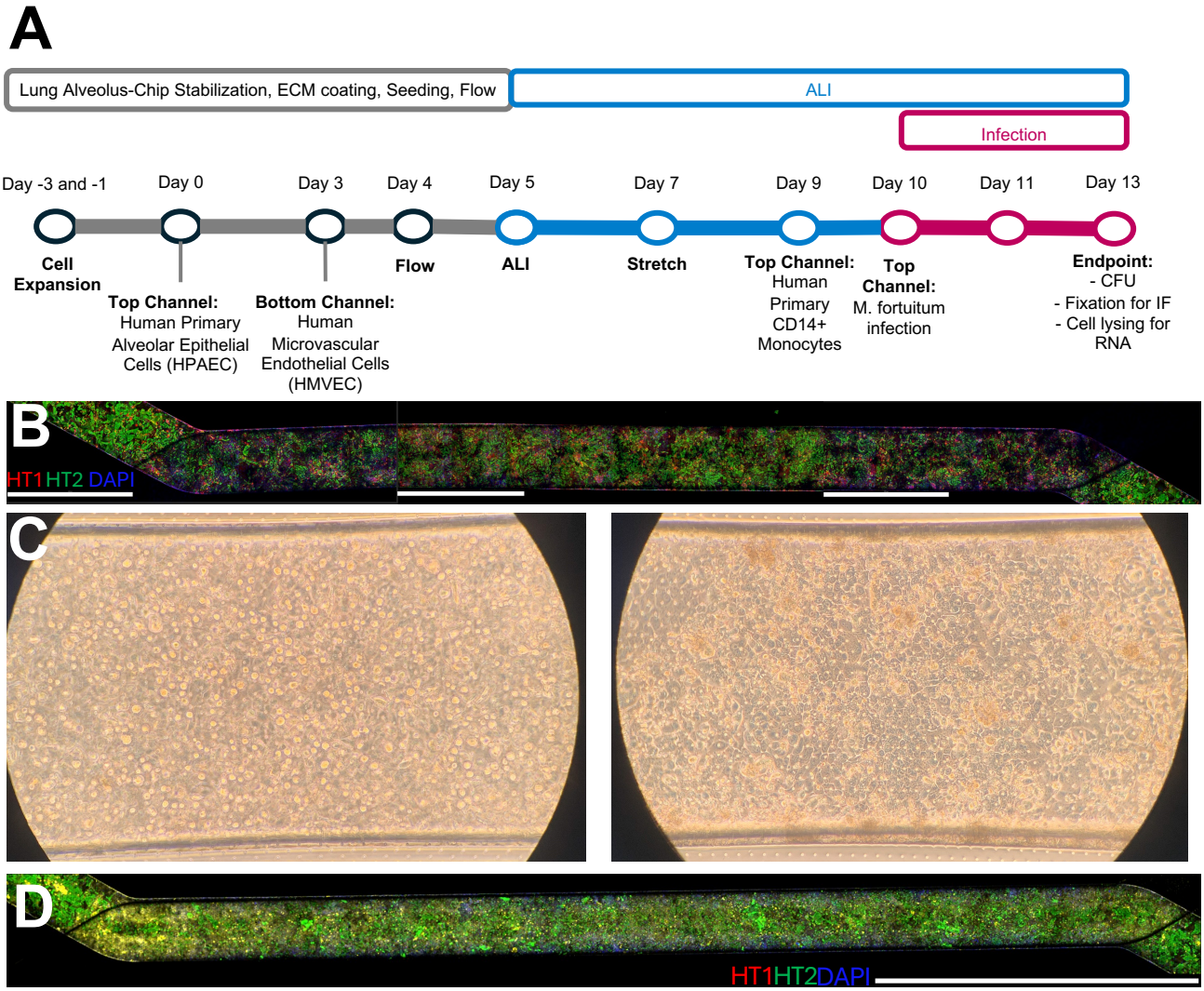

Supplemental Figure 2

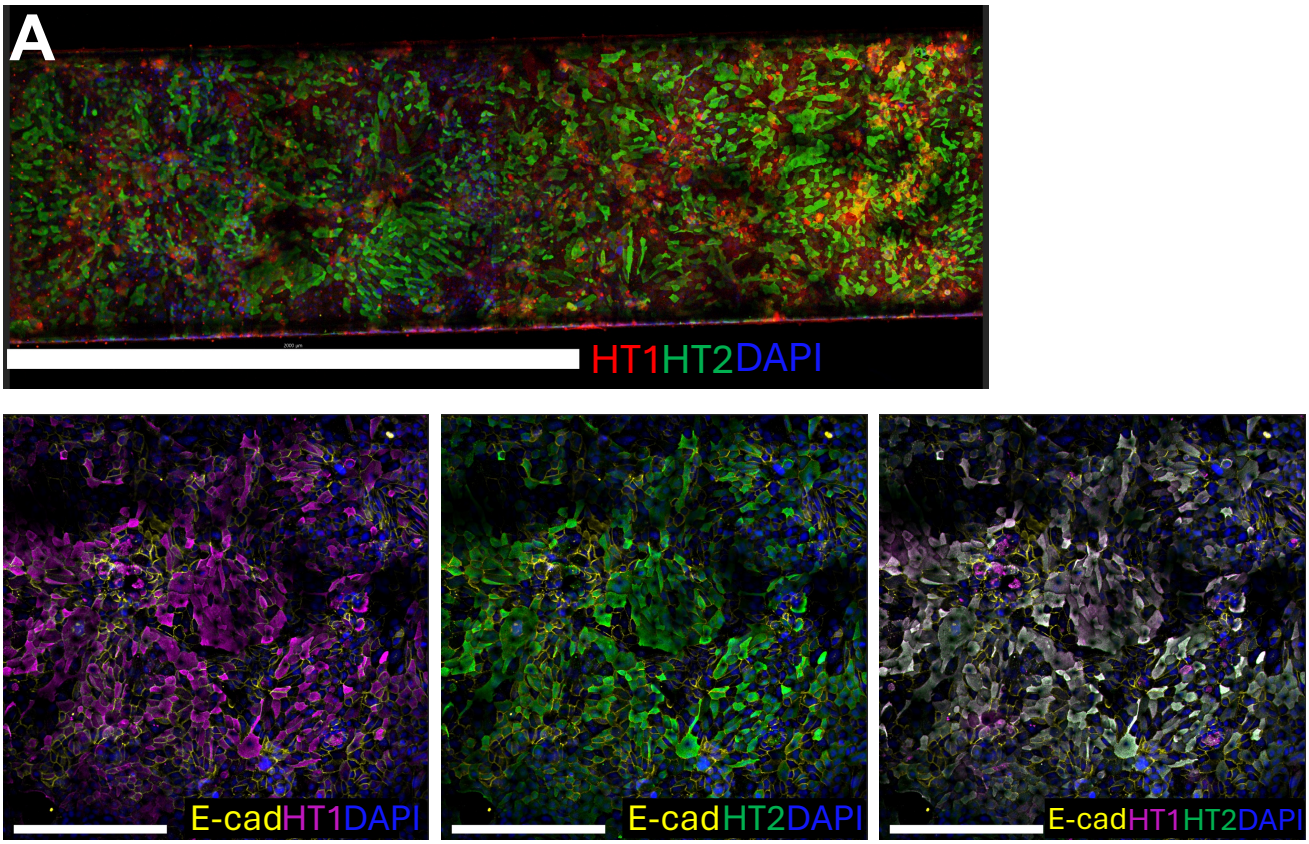
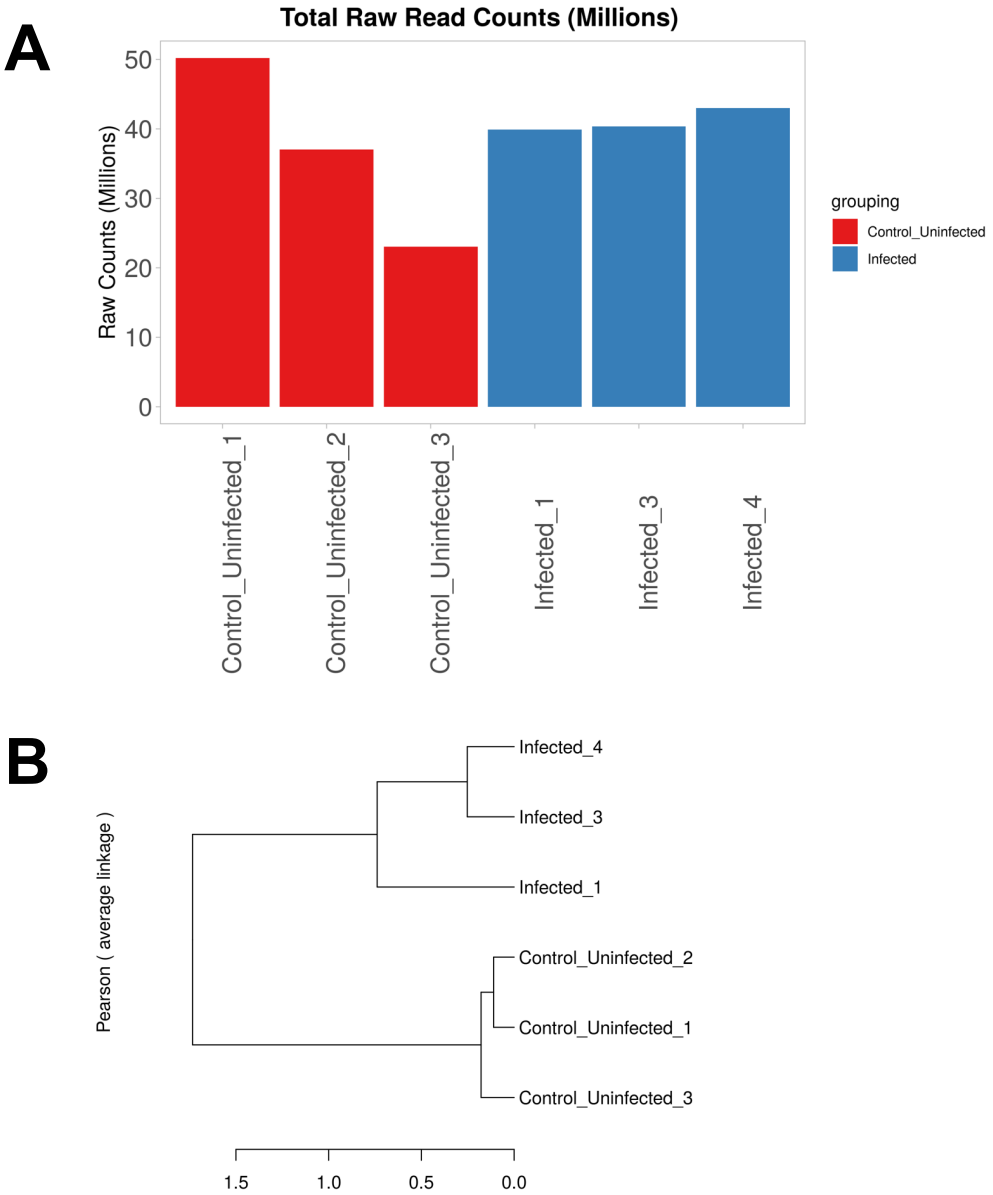
Supplemental Figure 3